

Correlating sparse sensing for large-scale traffic speed estimation: A Laplacian-enhanced low-rank tensor kriging approach

Tong Nie^a, Guoyang Qin^a, Yunpeng Wang^b, Jian Sun^{a,*}

^aDepartment of Traffic Engineering & Key Laboratory of Road and Traffic Engineering, Ministry of Education, Tongji University, Shanghai 201804, China

^bBeijing Key Laboratory for Cooperative Vehicle Infrastructure Systems and Safety Control, School of Transportation Science and Engineering, Beihang University, Beijing 100191, China

Abstract

Traffic speed is central to characterizing the fluidity of the road network. Many transportation applications rely on it, such as real-time navigation, dynamic route planning, and congestion management. Rapid advances in sensing and communication techniques make traffic speed detection easier than ever. However, due to sparse deployment of static sensors or low penetration of mobile sensors, speeds detected are incomplete and far from network-wide use. In addition, sensors are prone to error or missing data due to various kinds of reasons, speeds from these sensors can become highly noisy. These drawbacks call for effective techniques to recover credible estimates from the incomplete data. In this work, we first identify the issue as a spatiotemporal kriging problem and propose a Laplacian enhanced low-rank tensor completion (LETC) framework featuring both low-rankness and multi-dimensional correlations for large-scale traffic speed kriging under limited observations. To be specific, three types of speed correlation including temporal continuity, temporal periodicity, and spatial proximity are carefully chosen and simultaneously modeled by three different forms of graph Laplacian, named temporal graph Fourier transform, generalized temporal consistency regularization, and diffusion graph regularization. We then design an efficient solution algorithm via several effective numeric techniques to scale up the proposed model to network-wide kriging. By performing experiments on two public million-level traffic speed datasets, we finally draw the conclusion and find our proposed LETC achieves the state-of-the-art kriging performance even under low observation rates, while at the same time saving more than half computing time compared with baseline methods. Some insights into spatiotemporal traffic data modeling and kriging at the network level are provided as well.

Keywords: Network-wide traffic speed estimation, spatiotemporal correlation, kriging, graph Laplacian, large-scale traffic data, low-rank tensor completion

1. Introduction

Traffic speed is the central macroscopic quantity used to characterize the fluidity of the road network. Many applications in the transportation domain rely on the knowledge of traffic speed over the road network to support various dimensions of decision-making, such as real-time navigation, dynamic route planning, congestion management, pollution evaluation, and infrastructure optimization (Boriboonsomsin et al., 2012; Liebig et al., 2017; Liu et al., 2019; Han et al., 2020). With rapid advances in sensing and communication techniques, collecting traffic speed measurements becomes easier than ever: static sensors such as loop detectors are continuously logging vehicular speeds past a cross-section, while mobile sensors such as floating cars are chronicling speeds of their background traffic flow. In fluid mechanics' terminology, static sensors generate Eulerian measurements at fixed locations, while mobile sensors produce Lagrangian measurements following the flow as they move. To obtain a full picture of the network-wide traffic speed, either Eulerian measurements with dense sensor deployments or Lagrangian measurements with high vehicular penetration rates is desired, whereas in fact the reality is far from desirable.

One may see in reality that the static sensors often have a sparse coverage subject to high installation budget and maintenance costs and leave many road links undetected, thereby rendering low spatial resolution data that is hard to extend to the entire network. In the meanwhile, mobile sensors, which are mostly installed on commercial vehicle fleets like taxis, often result in a low penetration rate, which may render dubious speed estimation due to its biased representation of the population. In addition, sensors are prone to error or missing data due to various kinds of reasons such as equipment failure, communication outage, and out-of-service, speeds detected from these sensors can become highly noisy (Asif et al., 2016). These drawbacks combined imply that the sensing data is by no means ideal, and call for effective techniques to recover credible estimates from the

*Corresponding author. Address: Cao'an Road 4800, Shanghai 201804, China
Email address: sunjian@tongji.edu.cn (Jian Sun)

incomplete data. Fortunately, traffic speeds bounded in the road network are highly correlated in both space and time, and therefore pose a rich degree of redundancy (or low-rankness in a matrix or tensor theory’s term (Tan et al., 2013)) that undetected or erroneous speeds of some road links are recoverable by virtue of the correlation. In other words, sparse sensors are able to achieve a "collaborative perception" of traffic speeds of the undetected road links, when their intrinsic multi-dimensional correlations are effectively exploited (see Fig. 1).

Recent years have witnessed a vast array of studies investigating the problem of estimating traffic state on undetected road links (Meng et al., 2017; Zhang et al., 2020; Wu et al., 2021a; Lei et al., 2022). This problem is often cast into spatiotemporal traffic kriging (Wu et al., 2021a) in the literature. Unlike the traffic forecasting problem that aims at predicting future state of a road link given its historical state, spatiotemporal traffic kriging attempts to estimate the traffic state of an undetected road link without any historical state of that link; it instead needs to utilize measurements of other detected road links to complete the "spatial prediction." Kriging is therefore regarded as a special missing data imputation problem. *How to effectively utilize the correlation between undetected road links and other sparsely detected roads* is the core research question of this paper. Upon close inspection, we identify three-fold specific challenges:

First, correlation between speeds of the detected road links and speeds of the undetected ones can be arbitrary unless reasonable prior assumptions are made. Low-rankness is a widely-adopted general prior in literature to reflect linear correlation of traffic data over space and time (Tan et al., 2013; Asif et al., 2016; Chen et al., 2021a). However, low-rankness is not directly applicable to our kriging problem in which data are fully missing in some locations, as in this case, we can fill different sets of values to the missing data without changing the rank and the missing values therefore remain undetermined under the low-rankness assumption. Conceptually, low-rankness is not sufficient when imputing a space-time matrix with entire row or column missing. Additional regularization terms should be carefully considered to complement the low-rankness assumption (Bahadori et al., 2014; Yokota et al., 2018; Yamamoto et al., 2022).

Second, in addition to general correlation assumptions, exploiting the semantic spatiotemporal correlation of speeds is an necessary add-on. Since speed manifests microscopic traffic that is time-varying, dynamic, periodic, and spatially interdependent, in the meanwhile, spatial correlation is bounded on a graph instead of on a 2D plane, spatial correlation should consider the graph features (e.g., network topology) as well as traffic flow loaded on that graph (e.g., moving directions of traffic flow) (Li et al., 2017), exploiting spatio-temporal correlations is by no means trivial. Moreover, as a graph signal, traffic data features inherent time series characteristics such as continuity, periodicity, and stationary, providing another prior for ones to achieve time-varying recovery. Tailoring an effective kriging model to capture the multi-modal correlations of spatiotemporal traffic data is still an open question yet to be resolved.

Third, scalability of the kriging approach onto the network level is desired as it allows exploiting correlation of a wider scope of speeds over space with added accuracy. Moreover, when new measurements are collected, a kriging model with fast parametric update is preferable for an online estimation. To this end, computational efficiency is the key. However, classical Gaussian process (GP) based kriging doesn’t show scalability due to its computational complexity, while existing scalable tensor based imputation methods (Lu et al., 2019b; Chen et al., 2021a) are mainly designed for general data imputation problem, and are not applicable to the kriging task. Although Bayesian Gaussian kriging methods achieve flexible hyper-parameter tuning for spatiotemporal kriging (Lei et al., 2022; Chen et al., 2022b), its high consumption of time and memory in parametric learning of the Gaussian kernel inhibits itself from being scaled to the network level. Custom scalable solution algorithms need to be designed to maximize the kriging performance.

To tackle the challenges and realize a network-wide kriging of missing speed data for the undetected road links, we propose a Laplacian enhanced tensor completion (LETC) based kriging model to exploit multi-modal spatiotemporal correlations of traffic speeds, where three kinds of carefully chosen speed correlation – *temporal continuity*, *temporal periodicity* and *spatial proximity* – are simultaneously captured by assigning three forms of graph Laplacian. By integrating graph Laplacian into tensor completion model either explicitly or implicitly, LETC can leverage both global low-rankness property and local dependency informed by physical constraints at the same time. The framework contributes to the current literature in four aspects as follows:

1. We customize a new temporal graph Fourier transform (TGFT) based on temporal periodic graph Laplacian to encode the temporal periodicity of speeds. The TGFT complements the low-rankness assumption and enables parallelization of the tensor completion by a series of daily matrix in graph spectral domain.
2. We propose a novel diffusion graph regularization (DGR) to exploit spatial dependency on directed graphs. By modeling as random walkers on graphs, DGR considers the directed nature of traffic flows and closely connects with the graph diffusion process. Moreover, DGR features explicit physical explanations and encourages a low-pass propagation which is beneficial for reconstructing spatiotemporal traffic data.
3. We develop a general formulation of temporal consistency regularization (GTCR) to impose smoothness constraints on time slots within a kernel size. GTCR considers the causality of time series in a model-free manner and can directly convert into some previously developed temporal regularization terms.
4. To scale up the kriging on large-scale network, we speed up our model by randomized tensor singular value decomposition and conjugate gradient method. Experiments on million-level traffic datasets not only

reveal the superiority of LETC on both accuracy and computational efficiency, but also provide insights into handling large-scale kriging problem.

The rest of this article is organized as follows. Section 2 reviews related works about spatiotemporal kriging. Section 3 introduces basic concepts about tensor operations in this work and defines the tensor-based kriging problem. In Section 4, we propose the graph tensor-based kriging model and a scalable solution algorithm. In Section 5, we perform numerical experiments of the proposed approach on two public data sets, which is followed by model comparison, ablation studies, and sensitivity analysis. Section 6 concludes this work and provides future directions.

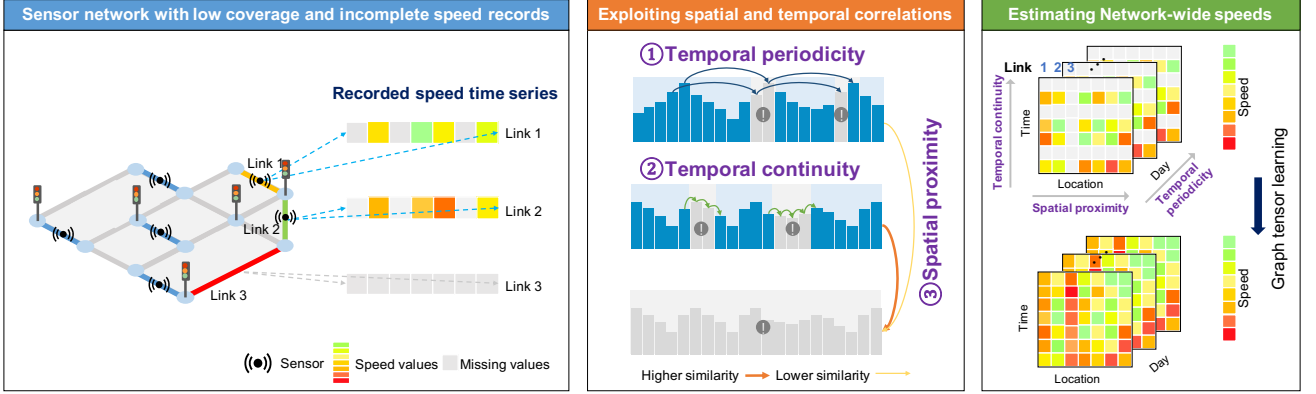


Figure 1: Illustration of spatiotemporal kriging problem. Take link 1, 2 and 3 as an example: link 1 and 2 record incomplete traffic speeds with missing time intervals, and link 3 are not equipped with a sensor so there is no historical record at all. The aim of spatiotemporal kriging is using the multi-dimensional spatial and temporal correlations (temporal continuity, temporal periodicity and spatial proximity) to infer the unmeasured locations (link 3) from the measured locations (link 1 and 2). In this figure, link 2 is physically closer to link 3 than link 1, so it is rational to assume link 2 and link 3 have stronger similarity.

2. Related work

Kriging is typically a regression problem for spatial modeling and interpolation of random fields based on covariance functions, which is a ubiquitous topic in geostatistics and usually associated with GP regression. Recently, kriging tasks have aroused great interests from different disciplines in machine learning community and many of these works can be viewed as special variants of kriging. In this section, we discuss kriging problems and summarize related solutions from a general perspective: spatial prediction with no historic data.

2.1. Graph regularized low-rank matrix and tensor completion based methods

In recommendation system community, graph regularized matrix completion/factorization models are commonly used for collaborative filtering tasks (Kalofolias et al., 2014; Rao et al., 2015; Strahl et al., 2020). The main purpose is to predict the unknown node values using side information about edges, which resembles the motivation of kriging. Kalofolias et al. (2014) first proposed a matrix completion model with graph Laplacian regularization. Rao et al. (2015) solved this problem in a scalable manner called graph regularized alternating least squares method, where conjugate gradient method was applied to update parameters. In the study of transportation, graph regularization is introduced either in space-time domain (Bahadori et al., 2014; Wang et al., 2018; Zhang et al., 2020; Yang et al., 2021), or graph spectral domain (Deng et al., 2021) to model spatial dependency. Among these works, Bahadori et al. (2014) proposed a tensor learning model for spatiotemporal co-kriging. The optimization problem was solved by greedy algorithm with orthogonal projections. Most of these works are developed for other data source and can not be directly transferred to our problem, as the unique characteristics of traffic speed should be taken into consideration.

2.2. Bayesian/probabilistic matrix factorization based method

Since kriging is a basic problem in GP modeling, some works combine GP priors with matrix factorization in a whole probabilistic framework to inference unknown data (Luttinen and Ilin, 2009; Zhou et al., 2012; Yang et al., 2018; Strahl et al., 2020). When graph Laplacian is specified as the kernel (covariance) function, this kind of model is equivalent to the graph regularized matrix factorization model. Most recently, Lei et al. (2022) proposed a Bayesian kernelized matrix factorization model for spatiotemporal traffic data imputation and kriging. Using a fully Bayesian treatment, this method can learn the hyper-parameters of graph kernels through resampling. One downside can not be overlooked is that the hyper-parameter sampling procedure is quite time-consuming. Therefore, there seems to be a trade-off between model scalability and flexibility.

2.3. Graph neural network based method

Graph convolution neural networks (GCN) has shown great potential for inductive modeling and achieved promising performances on kriging tasks (Appleby et al., 2020; Wu et al., 2021a,b; Liang et al., 2022). Appleby et al. (2020) first developed a kriging convolutional networks using K-nearest neighbor to reconstruct all the node values on a defined graph. Wu et al. (2021a) proposed an inductive GCN to model the spatial dependency and a random mask sample generation method was used for model training. However, both of these methods consider the sample over a specific observation time as individual or additional features, thus ignoring the temporal consistency. Liang et al. (2022) further improved the kriging performance of GCN by integrating an external attention mechanism and a temporal convolution network. Despite high accuracy has been achieved, training these elaborate GCN models is computationally very expensive and may require GPU hardware acceleration, which is prohibitive for large-scale problems.

2.4. Multi-way delay embedding (Hankelization) based methods

In the field of computer vision, kriging can be regarded as recovery of missing pixels along entire rows or columns of RGB images, i.e., a special image inpainting task (Yokota et al., 2018). Hankel matrix that bases on shift-invariant features of image is supposed to be a powerful tool for this issue. Yokota et al. (2018) proposed a Tucker tensor decomposition in multi-way delay-embedded (MDT) space method (aka., Hankelization) and extend the Hankel matrix to tensor. Yamamoto et al. (2022) further improved the scalability of Hankel tensor completion by using circulant MDT approximation. Although these pioneering works do not aim to solve spatiotemporal traffic kriging, the MDT based method has been applied to various transportation problems, such as traffic speed estimation from trajectories (Wang et al., 2021b), traffic data anomaly detection using RPCA (Wang et al., 2021a), and short-term traffic forecasting (Shi et al., 2020). In the context of spatiotemporal traffic data, there exists shift-invariant patterns in the time dimension, while this phenomenon is not distinctive in the space dimension. Without external spatial information, the MDT may produce erroneous kriging results.

3. Preliminaries and problem definitions

In this section, we first introduce some basic notation and preliminaries about tensor algebra. After that, we describe the spatiotemporal traffic speed kriging problem in the perspective of graph tensor learning framework.

3.1. Notation and basic concepts

Throughout this paper, we use the same notations as in (Kolda and Bader, 2009). Specifically, we adopt boldface capital letters to denote matrices, e.g., $\mathbf{M} \in \mathbb{R}^{M \times N}$, boldface lowercase letters, e.g., $\mathbf{a} \in \mathbb{R}^M$ to denote vectors, and scalars are denoted by lowercase letters, e.g., a . For a matrix \mathbf{M} , the i -th row and j -th column are abbreviated as $\mathbf{M}^i, \mathbf{M}_j$. A third-order tensor is denoted by calligraphic letter, e.g., $\mathcal{X} \in \mathbb{R}^{n_1 \times n_2 \times n_3}$, whose (i, j, k) -th entry is x_{ijk} , and we use the MATLAB notation $\mathcal{X}(i, :, :)$, $\mathcal{X}(:, i, :)$ and $\mathcal{X}(:, :, i)$ to denote the i -th horizontal, lateral and frontal slice, respectively. Specially, the frontal slice $\mathcal{X}(:, :, i)$ is denoted compactly as $\mathbf{X}^{(i)}$. A tubal fiber (mode-3 fiber) $\mathcal{X}(i, j, :)$ is obtained by fixing the first two indices and varying the third index. The inner product of two matrix is given by $\langle \mathbf{A}, \mathbf{B} \rangle = \text{Tr}(\mathbf{A}^T \mathbf{B})$, where $\text{Tr}(\cdot)$ signifies the matrix trace. The inner product of two third-order tensors is defined by $\langle \mathcal{A}, \mathcal{B} \rangle = \sum_{i,j,k} a_{i,j,k} b_{i,j,k}$, and the corresponding tensor Frobenius norm is $\|\mathcal{A}\|_F = \sqrt{\langle \mathcal{A}, \mathcal{A} \rangle}$.

For matrices, we introduce the reshaping and vectorization operation for efficient matrix-vector product. If $\mathbf{X} \in \mathbb{R}^{M \times N}$, then the vectorization of \mathbf{X} denoted by $\text{vec}(\mathbf{X})$ is an NM -by-1 vector obtained by stacking the columns of \mathbf{X} :

$$\text{vec}(\mathbf{X}) = \begin{bmatrix} \mathbf{X}(:, 1) \\ \vdots \\ \mathbf{X}(:, N) \end{bmatrix}. \quad (1)$$

Let $\mathbf{A} \in \mathbb{R}^{m \times n}$ and $m_1 n_1 = mn$, then the outcome of reshaping \mathbf{A} :

$$\mathbf{B} = \text{reshape}(\mathbf{A}, m_1, n_1) \quad (2)$$

is a m_1 -by- n_1 matrix defined by $\text{vec}(\mathbf{B}) = \text{vec}(\mathbf{A})$.

Graph Laplacian serves as a regularization term and has ubiquitous applications in geometric matrix factorization models (Kalofolias et al., 2014; Rao et al., 2015). Given an undirected and possibly weighted graph $\mathcal{G} = (\mathcal{N}, \mathcal{E}, \mathbf{W})$ with nodes \mathcal{N} and edges $\mathcal{E} \subseteq \mathcal{N} \times \mathcal{N}$ weighted with a non-negative weight matrix (adjacent matrix) \mathbf{W} , the graph Laplacian is calculated from the weight matrix:

$$\mathbf{Lap} = \mathbf{D} - \mathbf{W}, \mathbf{D} = \text{Diag}(\sum_{i'} w_{ii'}). \quad (3)$$

Invertible linear transform, is proved to be a flexible tool for different real data formatted as tensors (Lu et al., 2019b). Given an invertible linear transform, one can establish a transform induced tensor product (t-product) and tensor singular value decomposition (t-SVD) accordingly. Let $\mathbf{L} \in \mathbb{C}^{n_3 \times n_3}$ be an arbitrary invertible transform matrix (e.g., discrete Fourier transform (DFT), discrete cosine/sine transform (DCT/DST), unitary transform (UT) and graph Fourier transform (GFT)) that satisfies:

$$\mathbf{L}\mathbf{L}^H = \mathbf{L}^H\mathbf{L} = l\mathbf{I}_{n_3}, \quad (4)$$

where $l > 0$ is a constant and H is the conjugate transposition, then given a third-order tensor $\mathcal{X} \in \mathbb{R}^{n_1 \times n_2 \times n_3}$, the transform matrix is applied on each tube fiber $\mathcal{X}(i, j, :)$ along the **third-dimension** of \mathcal{X} , i.e.,

$$\bar{\mathcal{X}}(i, j, :) = \mathbf{L}\mathcal{X}(i, j, :), \quad (5)$$

which is equivalent to:

$$\bar{\mathcal{X}} = \mathcal{L}(\mathcal{X}) = \mathcal{X} \times_3 \mathbf{L}, \quad (6)$$

where we use $\mathcal{L}(\cdot)$ to denote the linear transform operator, $\bar{\mathcal{X}}$ is the transformed tensor, and \times_3 denotes the mode-3 product (Kolda and Bader, 2009). Similarly, the inverse transform is given by:

$$\mathcal{X} = \mathcal{L}^{-1}(\bar{\mathcal{X}}) = \bar{\mathcal{X}} \times_3 \mathbf{L}^H. \quad (7)$$

To give an intuitive example, when we adopt the DFT, the transformed tensor can be obtained by performing DFT of \mathcal{X} along the third-dimension, i.e., $\bar{\mathcal{X}} = \text{fft}(\mathcal{X}, [], 3)$ by using the MATLAB command `fft`.

The mechanism of transformed tensor completion is that by imposing transform along certain dimension, the whole tensor completion problem can be divided into solving a series of small-scale matrix completion problems for each frontal slice $\bar{\mathcal{X}}^{(i)}$, and their solutions are then concatenated through inverse transform. This treatment reduces the computational cost of tensor completion and enable us to perform it on large-scale data set by computing in parallel.

Like the product of two matrices, the product of two tensors induced by linear transform can be defined analogously.

Definition 1. (*t-product* (Lu et al., 2019b; Song et al., 2020)) Given any invertible transform \mathcal{L} , and $\mathcal{A} \in \mathbb{R}^{n_1 \times n_2 \times n_3}$ and $\mathcal{B} \in \mathbb{R}^{n_1 \times n_2 \times n_3}$, then the transform based t-product denoted as $\mathcal{C} = \mathcal{A} *_{\mathcal{L}} \mathcal{B}$, is defined such that $\bar{\mathcal{C}}^{(i)} = \bar{\mathcal{A}}^{(i)} \bar{\mathcal{B}}^{(i)}$, for $i = 1, \dots, n_3$.

Note that $\bar{\mathcal{C}}^{(i)} = \bar{\mathcal{A}}^{(i)} \bar{\mathcal{B}}^{(i)}$ can be denoted compactly using the block diagonal matrix. Def. 1 implies that the transform induced t-product can be performed by the matrix-matrix product in the transform domain. In the following sections, we will adopt this t-product to achieve some important tensor operations in the graph spectral domain.

3.2. Graph-regularized low-rank tensor learning for traffic speed kriging

Spatiotemporal traffic speed kriging can be treated as a special data imputation problem on a pre-specified graph so that we can model it through a tensor completion/learning method. Specifically, given an observation speed matrix $\mathbf{Z} \in \mathbb{R}^{(IK) \times J}$ whose rows correspond to IK uniformly distributed time points with I time intervals per day within K days, and columns correspond to sensors at J locations, the objective of spatiotemporal kriging in this paper can be described as learning the graph signals (node values) at unmeasured locations (entire columns) and missing time intervals (entire rows), given the observations and graph structure. This can be formulated as maximum of a posterior probability (MAP):

$$\hat{\mathbf{Z}} = \arg \max_{\mathbf{Z}} P(\mathbf{Z} | \mathbf{Z}_{\Omega}, \mathcal{G}_r, \mathcal{G}_c), \quad (8)$$

where $P(\cdot | \cdot)$ is the conditional probability function, Ω is the index where rows and columns are measured. \mathcal{G}_r and \mathcal{G}_c are prior information about rows and columns, i.e., temporal and spatial correlations in our case. From the perspective of tensor completion model, MAP is equivalent to the following form:

$$\begin{aligned} \min_{\mathcal{X}} \quad & \|\mathcal{X}\|_{\text{norm}} + \mathcal{R}_s(\mathcal{X}) + \mathcal{R}_t(\mathcal{X}), \\ \text{s.t.} \quad & \begin{cases} \mathbf{P} \odot \mathbf{Z} = \mathbf{P} \odot \mathbf{T}, \\ \mathcal{X} = \mathcal{F}(\mathbf{Z}), \end{cases} \end{aligned} \quad (9)$$

where $\|\mathcal{X}\|_{\text{norm}}$ is the tensor norm of \mathcal{X} to approximate the tensor rank, $\mathcal{R}_s(\cdot)$, $\mathcal{R}_t(\cdot)$ are spatial and temporal consistency regularization, respectively. \mathbf{P} is an indicating matrix whose entry is 1 when this data point is observed and 0 otherwise. \mathbf{T} is the partially observed matrix, \odot is the Hadamard product. Note that $\mathcal{F}(\cdot) : \mathbb{R}^{(IK) \times J} \rightarrow \mathbb{R}^{I \times J \times K}$ denotes a forward tensorization operator that converts the spatiotemporal matrix

into a third-order tensor of shape (time of day \times locations \times days) by stacking the ‘day’ dimension (Chen et al., 2021b). Conversely, the inverse matricization operator is denoted by $\mathcal{T}^{-1}(\cdot)$.

The first term in Eq. (9) encourages the tensor norm (Kolda and Bader, 2009) to be small (or rank to be low) which serves as a global soft constraints. Low-rank (small-norm) pattern can capture inherent redundancy and linearity of traffic data. In this work, we establish a new temporal graph Fourier transform based tensor nuclear norm (t-TNN). Moreover, it is not hard to find that the unmeasured rows and columns of a time-space matrix is manifested as some missing ‘slices’ of a tensor. Purely low-rank model is incapable of dealing with such ‘missing slices’ of tensor, because it is agnostic to the positional information (Nie et al., 2022). Therefore, the other two terms are designed for encoding side information about rows and columns, which are in fact local hard constraints. Overall, Eq. (9) is a simultaneous structured model that encourages sparsity of \mathcal{X} in the tensor singular value vector outer product space, and column-row wise sparsity of \mathbf{Z} in the spatial and temporal Laplacian eigenspaces. The proposed method mainly features tensor norm minimization and spatial-temporal regularization, which favors a globally low-rank and locally smooth solution.

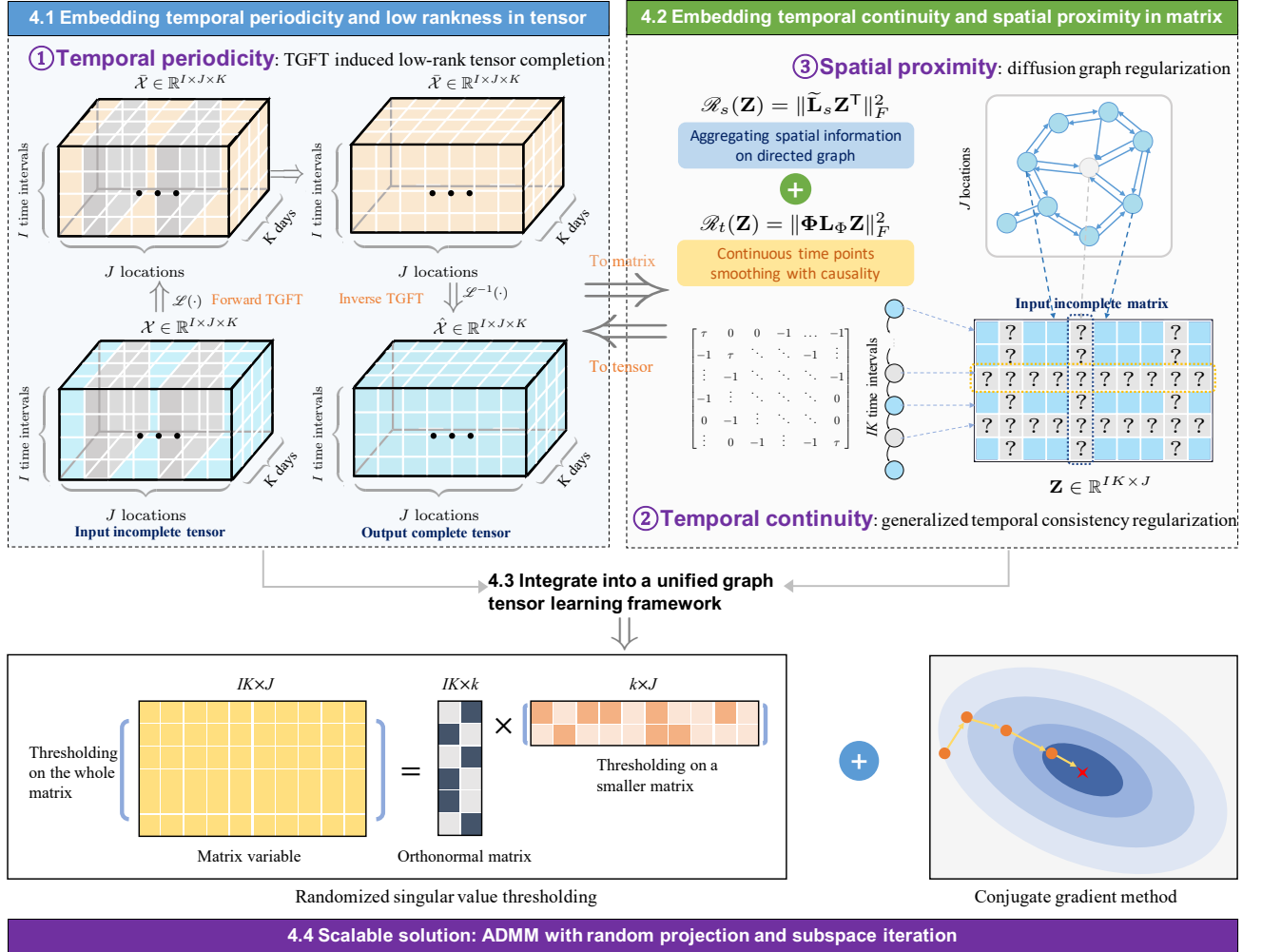


Figure 2: Illustration of proposed LETC framework. The whole method features three parts: embedding temporal periodicity and low rankness with temporal graph Fourier transform (in 4.1), modeling temporal continuity with a generalized temporal consistency regularization, and encoding spatial proximity with diffusion graph regularization (in 4.2 and 4.3). All three correlations are modeled by three types of graph Laplacian and integrated into a unified tensor learning model (in 4.4) and we obtain an efficient solution in 4.5 for large-scale problems.

4. Methodology

In this section, we first introduce a novel temporal graph Fourier transform (TGFT) on the basis on periodic graph Laplacian and the corresponding linear transform-induced tensor nuclear norm. Since then, we establish the temporal and spatial regularization with another two forms of graph Laplacian by generalized temporal consistency regularization (GTGR) and diffusion graph regularization (DGR), respectively. Finally, we formulate the integrated tensor completion model for traffic speed kriging and solve it in a highly scalable manner using the alternating direction method of multipliers (ADMM) with some valuable numeric techniques, i.e., randomized tensor singular value thresholding (r-tSVT) and conjugate gradient (CG). The proposed model is referred to as Laplacian enhanced tensor completion (LETC) model. The overall framework is shown in Fig. 2.

4.1. Embedding temporal periodicity and low rankness with temporal graph Fourier transform

As described in Section 3, invertible linear transform serves as an important role in scalable tensor completion methods. The most common transforms such as FFT, DCT, are adopted for image or video data (Lu et al., 2016, 2019b). Nevertheless, how to determine a knowledge-based transform for traffic data is still worthy to be considered. In the existing literature of transportation, Chen et al. (2021a) used a data-driven unitary transform which is obtained by the SVD of day-mode unfolding; Deng et al. (2021) performed GFT along the ‘location’ dimension to extract the graph information. Recall that we arrange the data in a tensor of (time of day \times locations \times days) format, if the linear transform is performed on the ‘days’ mode, dealing with each daily subproblem of transformed tensor separately may ignore the temporal periodicity of traffic data.

To take advantage of prior knowledge about spatiotemporal traffic data, we establish a novel temporal graph Fourier transform (TGFT) based on classical GFT. GFT has been widely applied into the graph spectral analysis and the emerging graph neural networks to capture the non-Euclidean relationships on graphs (Kipf and Welling, 2016). The basic GFT is defined as:

Definition 2. (GFT (Shuman et al., 2013)) Given a graph signal $\mathbf{f} \in \mathbb{R}^{n_3}$ and the graph Laplacian \mathbf{Lap} , the GFT of \mathbf{f} is

$$\bar{\mathbf{f}} = \text{GFT}(\mathbf{f}) = \mathbf{U}\mathbf{f}, \quad (10)$$

and the inverse operator is

$$\mathbf{f} = \text{iGFT}(\bar{\mathbf{f}}) = \mathbf{U}^H\bar{\mathbf{f}}, \quad (11)$$

where the transform matrix operator \mathbf{U} is obtained by the eigenvalue decomposition $\mathbf{Lap} = \mathbf{U}\mathbf{A}\mathbf{U}^H$.

Since the Laplacian matrix can be viewed as the Laplace operator on graphs, GFT is in fact a projection using the eigenvectors of the Laplacian matrix as the basis vectors (Sandryhaila and Moura, 2013). Similar to DFT, GFT is decomposing a graph signal into a series of graph signals with different degrees of smoothness. Therefore, graph signals in spectral domain also reflect different frequency components, and the eigenvalue can be analogous to frequency. The larger the eigenvalue, the greater the graph signal fluctuation.

To embed the multi-scale relationships of days and weeks, we establish the TGFT based on a temporal adjacent matrix that describes the day-to-day and day-of-week periodicity of ‘day’-mode slices. Since the eigenvalue decomposition of a symmetric matrix always leads to a set of orthogonal basis (Golub and Van Loan, 2013), we preserve the unitary property of GFT by establishing a symmetric adjacent matrix. Given a multivariate time series within D days, the temporal adjacent matrix $\mathbf{A}_t \in \mathbb{R}^{D \times D}$ is given as:

$$\begin{aligned} \mathbf{A}_t &= \mathbf{I}_D + \mathbf{P}_1 + \mathbf{P}_1^T + \sum_{n=1}^m (\mathbf{P}_T(n) + \mathbf{P}_T(n)^T), \\ \mathbf{P}_1 &= \begin{bmatrix} \mathbf{0}_{1 \times (D-1)} & 0 \\ \omega_1 \mathbf{I}_{D-1} & \mathbf{0}_{(D-1) \times 1} \end{bmatrix}, \\ \mathbf{P}_T(n) &= \begin{bmatrix} \mathbf{0}_{nT \times (D-nT)} & \mathbf{0}_{nT \times nT} \\ \omega_T \mathbf{I}_{D-nT} & \mathbf{0}_{(D-nT) \times nT} \end{bmatrix}, \end{aligned} \quad (12)$$

where T is the length of a period and m is the total number of periods within D days, ω_1 and ω_T denote the similarity weights of day-to-day and day-of-week patterns respectively, which can be chosen according to the daily variations of traffic states. In practice, ones can possibly consider setting a decaying factor $\beta \in (0, 1)$ for ω_T to take into account the effect of long time sequence, e.g., $\omega_T(n) = \beta(1 - \beta)^n \omega_T(1)$. Moreover, consider the fact that traffic patterns could be different among weekends and weekdays, we can incorporate this heterogeneity by simply modifying \mathbf{P}_1 as follows:

$$\begin{aligned} \mathbf{P}'_1 &= \begin{bmatrix} \mathbf{0} & 0 \\ \text{BDiag}(\mathbf{H}_{T \times T}) & \mathbf{0} \end{bmatrix}, \\ \mathbf{H} &= \text{Diag}(\underbrace{\omega_1, \dots, \omega_1}_{T-2T_w+1}, \underbrace{\omega_2, \dots, \omega_2}_{2T_w-1}). \end{aligned}$$

where $\text{BDiag}(\cdot)$ constructs a block diagonal matrix, T_w is the number of different daily patterns, e.g., $T_w = 2$ for weekends, and ω_2 is the corresponding weights.

Eq. (12) depicts the graphical model in Fig. 3 (a), and it has intuitive explanation: the first term \mathbf{I}_D represents the self-loop of each node itself, \mathbf{P}_1 denotes the first-order neighborhood, i.e., the adjacent two days, and $\mathbf{P}_T(n)$ signifies the neighbors in n -th period, which forms the nT -th lower main diagonal. The transpose terms are added to make \mathbf{A}_t undirected and symmetric. Fig. 3 (b) gives an example with $D = 6$ and $T = 3$.

\mathbf{A}_t directly connects two ‘day’-mode slices with weight being one if two days are consecutive or the same day of a week. After computing \mathbf{A}_t , we can obtain a temporal periodic Laplacian \mathbf{L}_t using Eq. (3). Since \mathbf{A}_t is nonnegative and symmetric, then the Laplacian \mathbf{L}_t is thus symmetric and semi-positive definite. Moreover, as \mathbf{L}_t is real-valued, the resulted eigendecomposition $\mathbf{L}_t = \mathbf{U}_t \mathbf{\Lambda} \mathbf{U}_t^T$ is also real-valued. Different from FFT that

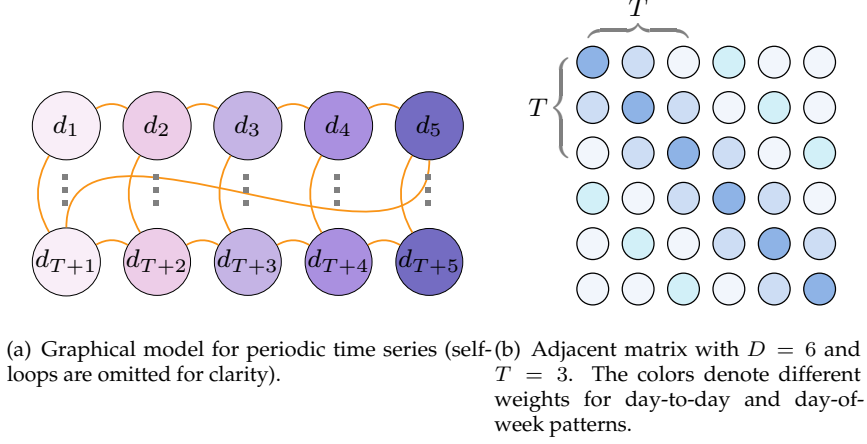


Figure 3: Temporal undirected graphical models with period T . Each node represents the data of a day.

operates in the complex domain, TGFT enables the tensor operations in real-valued graph spectral domain. It is obvious that the TGFT operator \mathbf{U}_t holds the property in Eq. (4) thus the forward and backward transform can be implemented for tensors using Eq. (6) and Eq. (7).

Each tubal fiber $\mathcal{X}(i, j, :)$ of the transformed tensor describes the graph signal at the i -th time interval in the j -th location within K days, and all fibers are controlled by a single temporal Laplacian. After performing TGFT, we are allowed to tackle the transformed matrix optimization subproblem for each day (which will be discussed in Section 4.5.1) and the ‘day-to-day’ and ‘day-of-week’ correlations (i.e., temporal periodicity) are encoded in the whole transformed tensor (see Fig. 2).

Compared with GFT performed on the ‘location’ mode in (Deng et al., 2021), when there exists a large number of sensors at network level ($J \gg I, K$), the proposed TGFT can split the original problem into much fewer (K) subproblems with well scalability, rather than J in original GFT.

Once we assign TGFT as the linear transform in Eq. (4), the corresponding transform based tensor nuclear norm (t-TNN) and tensor-tensor product (t-product) can be given as follows.

Definition 3. (t-TNN (Lu et al., 2019b; Song et al., 2020)) *The t-TNN of a tensor $\mathcal{A} \in \mathbb{R}^{n_1 \times n_2 \times n_3}$ is the sum of the nuclear norms of all frontal slices of $\bar{\mathcal{A}}$, i.e.,*

$$\|\mathcal{A}\|_{t*} = \sum_{i=1}^{n_3} \|\bar{\mathbf{A}}^{(i)}\|_* = \|\tilde{\mathbf{A}}\|_*, \quad (13)$$

where $\|\cdot\|_*$ denotes the matrix nuclear norm, $\tilde{\mathbf{A}} \in \mathbb{R}^{n_1 n_3 \times n_2 n_3}$ is the block diagonal matrix of $\bar{\mathcal{A}}$ with its i -th block on the diagonal as the i -th frontal slice of $\bar{\mathcal{A}}$:

$$\tilde{\mathbf{A}} = \begin{bmatrix} \bar{\mathbf{A}}^{(1)} & & & \\ & \bar{\mathbf{A}}^{(2)} & & \\ & & \ddots & \\ & & & \bar{\mathbf{A}}^{(n_3)} \end{bmatrix}.$$

It has been proved that the above t-TNN is the convex envelope of the tensor tubal rank (Lu et al., 2019b; Song et al., 2020). The motivation behind using t-TNN in this work is to preserve the low-rank property of traffic data tensor as well as to reduce the computational cost as much as possible. Traditionally, the tensor rank is approximated by the sum of nuclear norm or Schatten p -norm of all unfolding matrices (Chen et al., 2021b; Nie et al., 2022), and the SVD needs to be conducted on all unfolding matrices. Consider that we assume $n_2 \gg n_1 > n_3$ for large-scale problems, this yields time complexity of $\mathcal{O}(n_1^2 n_2 n_3 + n_1 n_2 n_3 \min\{n_2, n_1 n_3\} + n_1 n_2 n_3^2)$ in total. While under the definition of t-TNN, SVD only needs to be computed on n_3 frontal slices of size $n_1 \times n_2$ and the time complexity reduces to $\mathcal{O}(n_1^2 n_2 n_3)$.

Induced by TGFT, we are allowed to perform t-TNN optimization in the domain of graph spectral, and obtain the output tensor in original space-time domain through inverse TGFT. This can be viewed as a feature augmentation by coordinate transformation, where a new subspace benefiting low-rankness is chosen. Additionally, by embedding the relationships between data of days, ‘day’-mode slices with similar components on graph Fourier basis are encouraged to share close patterns.

Performing tensor nuclear norm minimization (i.e., Eq. (13)) can solve the missing data imputation problem with element-like or fiber-like missing patterns (Nie et al., 2022). However, when there exists entire missing slices of a tensor, using pure low-rank assumption could be undesirable as the original tensor structure is not sensitive

to the permutation of tensor fibers. Therefore, the key to model kriging as a tensor completion problem is to exploit side information as physic guidance. In the following sections, we construct temporal continuity and spatial proximity regularization by developing a generalized temporal consistency regularization and a novel diffusion graph regularization respectively.

4.2. Modeling time series continuity with generalized temporal consistency regularization

In time dimension, we establish the ‘time-of-day’ relationship (i.e., temporal continuity) explicitly by extra regularization, because the ‘day-to-day’ and ‘day-of-week’ correlations are already embedded in the transformed tensor by TGFT. For traffic data imputation and forecasting problems, some elaborate time series models such as vector autoregressive (Yu et al., 2016; Chen et al., 2021b), long-short term memory neural network (Yang et al., 2021), quadratic variation (Chen et al., 2021a), are adopted to capture complex and long-term temporal dynamics. While at the same time, more computational burdens are brought to train such temporal models. Traditional Toeplitz temporal regularization fails to capture multi-hop dependencies. Besides, recent study (Chen et al., 2022a) has demonstrated that temporal relationships can be represented by graph of time series, and the Laplacian kernel can be used as a local smoothness regularization, which features both accuracy and efficiency. In their work, undirected and circulant graphs are adopted to characterize the time series dependencies.

Inspired by (Chen et al., 2022a; Singh et al., 2016), we define a general form of temporal consistency regularization in the context of directed graph Laplacian, which is a general case of some temporal smoothness penalty, e.g., Toeplitz matrix. To reflect the causality of time series, directed temporal graph representing the dependent relationships of time series is constructed by first defining a temporal kernel \mathbf{k}_τ parameterized by kernel size τ :

$$\mathbf{k}_\tau = (\tau, \underbrace{-1, \dots, -1}_\tau, 0, \dots, 0)^\top \in \mathbb{R}^T, \quad (14)$$

where τ determines the window size of temporal smoothness. Then its circulant matrix $\mathcal{C}(\mathbf{k}_\tau)$ is in fact the Laplacian (Singh et al., 2016) of a directed and unweighted temporal graph (see Fig. 4):

$$\mathcal{C}(\mathbf{k}_\tau) = \mathbf{L}_\Phi = \begin{bmatrix} \tau & 0 & 0 & -1 & \dots & -1 \\ -1 & \tau & \ddots & \ddots & -1 & \vdots \\ \vdots & -1 & \ddots & \ddots & \ddots & -1 \\ -1 & \vdots & \ddots & \ddots & \ddots & 0 \\ 0 & -1 & \vdots & \ddots & \ddots & 0 \\ \vdots & 0 & -1 & \vdots & -1 & \tau \end{bmatrix}_{T \times T}. \quad (15)$$

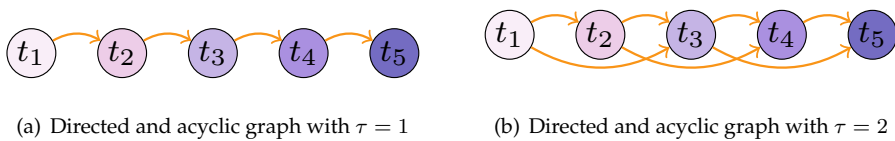


Figure 4: Temporal graphical models with directed and acyclic edges. Each node represents a time point of a series. In these examples, $\mathcal{C}(\mathbf{k}_1)$ and $\mathcal{C}(\mathbf{k}_2)$ are their respective directed Laplacian matrices.

Finally, given an input graph signal $\mathbf{Z} \in \mathbb{R}^{T \times N}$, GTCR is formulated as:

$$\mathcal{R}_t(\mathbf{Z}) = \|\Phi \mathbf{L}_\Phi \mathbf{Z}\|_F^2, \quad (16)$$

where Φ is a truncation operator defined as:

$$\Phi = [\mathbf{0}_{(T-\tau) \times \tau} \quad \mathbf{I}_{T-\tau}]. \quad (17)$$

This operator is used to remove the first τ rows in $\mathcal{C}(\mathbf{k}_t)$, thereby avoiding the loops in the temporal graph.

Remark 1. Eq. (16) is a general form of temporal regularization and can degrade into many widely used regularization in the literature. For example,

1. when $\tau = 1$ and $\Phi = \mathbf{I}_T$, it yields the traditional one-order Toeplitz temporal regularization like in (Wang et al., 2018);
2. when $\mathbf{L}'_\Phi = \mathbf{L}_\Phi \mathbf{L}_\Phi^\top$ and $\Phi = \mathbf{I}_T$, it leads to the circulant and symmetric Laplacian in (Chen et al., 2022a);

3. when $\tau = 1$ and $\Phi = [\mathbf{0}_{(T-1) \times 1} \ \mathbf{I}_{T-1}]$, it becomes the quadratic variation norm in (Chen et al., 2021a).

The function of GTCR is to make consecutive time points within the kernel size (time window) to be smooth, and Eq. (16) only imposes this smoothness penalty along the direction of time lapse, without assumption of cyclicity. The larger the kernel size, the longer the temporal receptive field. This model-free technique could provide a simple but efficient tool for modeling varying degrees of temporal dependencies along ‘time interval’ dimension.

4.3. Modeling spatial proximity with diffusion graph regularization

As for spatial dimension, symmetric graph Laplacian derived from symmetric adjacent matrix is the most commonly used spatial regularization in the literature to perform kriging (Bahadori et al., 2014; Kalofolias et al., 2014; Rao et al., 2015; Wang et al., 2018; Zhang et al., 2020; Yang et al., 2021; Lei et al., 2022). Most of these approaches are limited to the analysis of traffic data lying on undirected graphs. However, traffic network is in essence a directed graph whose edge reflects the directional movement of traffic flow. To operate on such directed graphs (see Fig. 5), existing works usually construct a symmetric adjacent matrix by bool sum or simple average of the asymmetric adjacent and its transpose.

Despite of its simplicity, recent graph neural network studies (Li et al., 2017; Wu et al., 2019) reveal that such symmetrization could bring in extra errors because of the ignore of traffic operation directions. To tackle this issue, we propose a new diffusion graph regularization that can be applied for directed graph structures.

Since Eq. (3) is defined for symmetric adjacent matrix and Laplacian, the first modification is to use the in-degree or out-degree matrix (Chung, 2005) of asymmetric adjacent matrix to compute Laplacian. Therefore, the resultant graph Laplacian is also asymmetric. Then, based on physical sensor graphs, we assume that the spot speed recorded by a static detector (e.g., loop sensor) tends to be similar with the values of its upstream or downstream neighbor sensors that determined by the graphical structure of traffic network. Thus we treat all sensors as nodes $\mathcal{V} = \{v_1, \dots, v_n\}$ and the relational connectivity of them as directed edges with asymmetric weight matrix \mathbf{A}_s representing similarity intensities.

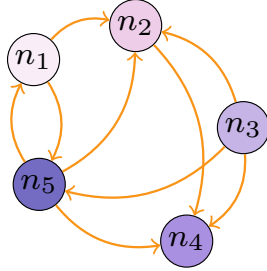


Figure 5: Spatial graphical models with directed edges. Each node represents a sensor on the network and edge direction reflects the moving direction of traffic flow.

In this work, we calculate the weights matrix by Gaussian kernel function:

$$a_{ij}^s = \begin{cases} \exp\left(-\left(\frac{\text{dist}(v_i, v_j)}{\sigma}\right)^2\right) & \text{if a directed edge exists from } v_i \text{ to } v_j, \\ 0 & \text{otherwise,} \end{cases} \quad (18)$$

where $\text{dist}(v_i, v_j)$ is the physical distance between sensor v_i and v_j , which can be obtained from the travel distance or the coordinate position; σ is a kernel hyper-parameter which can be chose as the standard deviation of the distance matrix.

By performing Eq. (3), the in-degree or out-degree graph Laplacian of sensor graph is derived by $\mathbf{L}_s = \text{Diag}(\sum_i \text{or } \sum_j a_{ij}^s) - \mathbf{A}_s$, and finally the proposed DGR for spatial modeling can be formulated as following:

$$\mathcal{R}_s(\mathbf{Z}) = \sum_j \left\| \frac{1}{d_j} \sum_i a_{ij}^s \mathbf{z}_i - \mathbf{z}_j \right\|_2^2 = \|\tilde{\mathbf{A}}_s \mathbf{Z}^T - \mathbf{Z}^T\|_F^2 = \|\tilde{\mathbf{L}}_s \mathbf{Z}^T\|_F^2, \quad (19)$$

where d_j is the j -th diagonal element of in-degree (or out-degree) matrix \mathbf{D} , $\tilde{\mathbf{A}}_s = \mathbf{D}^{-1} \mathbf{A}_s$ is the normalized adjacent matrix, and $\tilde{\mathbf{L}}_s = \mathbf{I} - \mathbf{D}^{-1} \mathbf{A}_s$ is the random-walk normalized Laplacian.

For a graph \mathcal{G} with non-negative weights and no isolated nodes, $\mathbf{D}^{-1} \mathbf{A}_s$ becomes the transition matrix of a random walker (Chung, 2005) on \mathcal{G} , thereby producing a diffusion process. Note that Eq. (19) is a natural generalization of graph Laplacian regularization on directed graphs. By letting $\tilde{\mathbf{L}} = \mathbf{L} \mathbf{L}^T$, DGR yields exactly the original form for undirected graphs, e.g., $\text{Tr}(\mathbf{Z} \mathbf{L} \mathbf{Z}^T)$.

By extending the spatial regularization to directed graphs, we can shed light on the natural connections between the proposed DGR and other diffusion kernels that are successfully applied in graph convolution based models (Kondor and Lafferty, 2002; Xu et al., 2020). Note that the core of Eq. (19) is the *forward propagation* operation, i.e., $\tilde{\mathbf{A}}_s \mathbf{Z}^\top$. Formally, we can re-write it in a more general view:

$$f(\mathbf{Z}^\top | h(\tilde{\mathbf{A}}_s)) = h(\tilde{\mathbf{A}}_s) \mathbf{Z}^\top, \quad (20)$$

where $h(\cdot) : \mathbb{R}^{N \times N} \rightarrow \mathbb{R}^{N \times N}$ is a diffusion function that determines the behaviors of random walker on graphs. Three specific formulations of diffusion functions are discussed in this paper, they are:

- High-order diffusion kernel:

$$h(\tilde{\mathbf{A}}_s) = \tilde{\mathbf{A}}_s^K, \quad (21)$$

where K is the diffusion steps;

- Personalized Page Rank (PPR) kernel (Page et al., 1998):

$$h(\tilde{\mathbf{A}}_s) = \sum_{K=0}^{\infty} \alpha (1 - \alpha)^K \tilde{\mathbf{A}}_s^K, \quad (22)$$

where $\alpha \in (0, 1)$ is the teleport probability;

- Heat diffusion kernel (Kondor and Lafferty, 2002):

$$h(\tilde{\mathbf{A}}_s) = \sum_{K=0}^{\infty} e^{-t} \frac{t^K}{K!} \tilde{\mathbf{A}}_s^K, \quad (23)$$

where t is the diffusion time.

It should be noted that in existing studies diffusion kernels are mostly used as an aggregation operation combined with learnable parameters to serve as underlying functions of graph machine learning models (Li et al., 2017; Wu et al., 2019). Few of them have paid attention to its role in acting as a graph constraint.

By introducing the above diffusion kernels in Eq. (19), DGR benefits from the exploration of high-order and hierarchical structures, which can explain most of the success of an effective kriging model.

Furthermore, having carefully inspected the roles of DGR for modeling spatial-temporal traffic data on graphs, we find that there are two physics-informed ways to understand the behaviors of it from the perspective of: 1) manifold learning, and 2) graph diffusion equation, which are less discussed in previous studies based on typical graph Laplacian constraints.

First, let us start with the well-known Laplacian regularized least-square problems (LapRLS) (Belkin and Niyogi, 2004):

$$f^* = \arg \min_{f \in \mathcal{H}} \ell(f(\mathbf{x}) - \mathbf{y}) + \gamma \|f\|_{\mathcal{H}}^2, \quad (24)$$

where \mathbf{x} and \mathbf{y} are training data and labels, $\|f\|_{\mathcal{H}}^2$ is a Laplacian kernel induced norm in \mathcal{H} , and ℓ is a loss function. LapRLS attempts to learn a function f from among a hypothesis space of functions \mathcal{H} , with the aim to predict the true labels as well as minimizing the Laplacian manifold regularization. Consider the fact that spatiotemporal traffic data tends to be low-rank in space-time domain and *low-frequency* in spectral domain (Liu and Zhang, 2022; Chen et al., 2022a), we can instantiate Eq. (24) from a matrix view with the following objective:

$$\min_{\bar{\mathbf{X}}} \|\mathbf{P} \odot (\bar{\mathbf{X}} - \mathbf{X})\|_{\mathbb{D}}^2 + \text{Tr}(\bar{\mathbf{X}}^\top \mathbf{L} \bar{\mathbf{X}}), \quad (25)$$

where $\|\cdot\|_{\mathbb{D}}$ means the augmented degree matrix induced norm denoted by $\|\mathbf{x}\|_{\mathbb{D}} = \sqrt{\mathbf{x}^\top \tilde{\mathbf{D}} \mathbf{x}}$ (Nt and Maehara, 2019). The first term measures the reconstruction loss on the observed data weighted by the importance of different nodes. The second term is the graph Dirichlet energy which represents the smoothness of graph signals. By optimizing Eq. (25) we can obtain an approximated graph signal with low-frequency components. The closed form solution is given by (detailed derivation is given in Appendix D):

$$\bar{\mathbf{X}} = (\mathbf{I} + \tilde{\mathbf{L}}_s)^{-1} \mathbf{X}. \quad (26)$$

If we consider the first-order Taylor approximation of it, we can obtain:

$$\bar{\mathbf{X}} := (\mathbf{I} - \tilde{\mathbf{L}}_s) \mathbf{X} = \tilde{\mathbf{A}}_s \mathbf{X}, \quad (27)$$

which leads to the propagation term in Eq. (19) exactly. In this sense, we can find that DGR explicitly encourages a low-frequency solution in graph spectral domain which is desirable for spatiotemporal traffic data and can be treated as a ‘low-pass’ filter (Nt and Maehara, 2019).

Second, we can present an exposition from another perspective by revisiting the (heat) diffusion equation on graphs (Chamberlain et al., 2021). Consider a diffusion process that depicts the evolution of graph signal matrix \mathbf{X} over time:

$$\frac{\partial \mathbf{X}(t)}{\partial t} = \text{div}(\mathbf{G}(\mathbf{X}(t), t) \odot \nabla \mathbf{X}(t)), \quad (28)$$

where \mathbf{G} is chosen to ensure $\mathbf{A} \odot \mathbf{G}$ to be a right random walk matrix, and $\text{div}(\cdot)$, ∇ are the divergence and gradient operators respectively. We can discrete Eq. (28) with a relatively small step h using explicit Euler scheme (Chamberlain et al., 2021) and plugging in the expressions of $\text{div}(\cdot)$, ∇ on graphs:

$$\mathbf{X}(kh) = \mathbf{X}((k-1)h) - h\tilde{\mathbf{L}}_s \mathbf{X}((k-1)h) := \tilde{\mathbf{L}}_s \mathbf{X}((k-1)h). \quad (29)$$

Eq. (29) means that if we treat the data flows from one node to another one with a step-by-step propagation, multiplying $\tilde{\mathbf{L}}_s$ with \mathbf{X} denotes a forward diffusion of all data points on the graph at the current state. More importantly, by performing Eq. (29) successively and filling the observed values to \mathbf{X} at each step, which are already embedded in our ADMM algorithm in section 4.5, we allow the data propagates from observed ones to unobserved ones as well as among the unknown nodes, which forms a bounded (heat) diffusion process with finite steps on graph.

Remark 2. DGR can also be implemented on both directions of diffusion. For example, if we consider inflow and outflow at the same time, Eq. (19) can be formulated as:

$$\mathcal{R}_s(\mathbf{Z}) = \|\tilde{\mathbf{L}}_f \mathbf{Z}^\top + \tilde{\mathbf{L}}_b \mathbf{Z}^\top\|_F^2.$$

In this case, $\tilde{\mathbf{L}}_f = \mathbf{I} - \mathbf{A}_s / \text{rowsum}(\mathbf{A}_s)$, $\tilde{\mathbf{L}}_b = \mathbf{I} - \mathbf{A}_s^\top / \text{columnsum}(\mathbf{A}_s)$ are forward and backward transition Laplacian respectively. Additionally, DGR can be applied to many other graph-based tasks, e.g., network-wide traffic forecasting.

The intuition behind Eq. (19) is to first aggregate neighborhood features according to the information passing mechanism on graph, then impose a column-wise smoothness to make locally connected nodes have similar node values. This process shares similar ideas with the graph diffusion convolution network (Li et al., 2017; Wu et al., 2019), while we only consider one-step random walk. This operation can encode the local spatial dependency and impute the unknown node values by borrowing referable information from measured ones.

Moreover, one can find that both $\mathcal{R}_t(\mathbf{Z})$ and $\mathcal{R}_s(\mathbf{Z})$ has similar form of Laplacian representation. Both of them encourage column or row wise sparsity of \mathbf{Z} in the spatial and temporal Laplacian eigenspaces, representing the relationships of sensors on two individual dimensions.

4.4. Low-rank tensor learning with Laplacian enhancement

Having introduced all the components of model above, we now integrate the low-rank optimization part with spatial and temporal regularization in a unified tensor learning framework, making Eq. (9) the following specific form:

$$\begin{aligned} \min_{\mathcal{X}} \|\mathcal{X}\|_{t*} + \frac{\lambda_1}{2} \|\tilde{\mathbf{L}}_s \mathbf{Z}^\top\|_F^2 + \frac{\lambda_2}{2} \|\Phi \mathbf{L}_\Phi \mathbf{Z}\|_F^2 \\ \text{s.t. } \mathbf{P} \odot \mathbf{Z} = \mathbf{P} \odot \mathbf{T}, \mathcal{X} = \mathcal{T}(\mathbf{Z}), \end{aligned} \quad (30)$$

where λ_1 and λ_2 are model hyper-parameters to balance the scale of t-TNN and extra regularization, $\mathcal{X} \in \mathbb{R}^{I \times J \times K}$ or $\mathbf{Z} \in \mathbb{R}^{(IK) \times J}$ are the target variables.

Eq. (30) is a transductive semi-supervised learning model, which means that the model training and inference process are in the same stage. The motivation of using the tensorization operator \mathcal{T} to connect tensor with matrix is that we can impose regularization on columns and rows of the spatiotemporal matrix directly, and utilize the t-TNN of tensor to achieve ‘low-rank’ in the graph spectral domain simultaneously, without pre-specified rank parameter as in (Kolda and Bader, 2009). Another important reason is that the optimization problem of typical tensor completion is usually coupled (Liu et al., 2013), and we can decouple it using the connection between tensor and matrix with no need for introducing extra auxiliary variables.

Remark 3. It can be seen that Eq. (30) contains the ‘location’ and ‘time-of-day’ mode Laplacian matrices explicitly, and keeps the ‘day’ mode Laplacian implicitly in the t-TNN. This consideration is twofold: (1) We treat ‘day-to-day’ and ‘day-of-week’ as global features, which are complementary to low-rankness; (2) As TGFT is performed on the ‘day’ dimension for all locations, we can preserve the periodic structure of traffic data by ‘day’ mode Laplacian, which is a natural and straightforward choice. Ones can also impose Laplacian regularization on three unfolding matrices in turn, as in (Sofuoglu and Aviyente, 2022). However, this treatment could bring extra computational complexity and may cause over-smoothing problem.

4.5. Scalable solution with ADMM

It can be seen that after incorporating the spatial and temporal regularizers the model updating process confronts with more computational overhead, because both the Toeplitz and graph Laplacian are item-by-item smoothing operators and more computations are introduced. A traditional choice for solving tensor completion problem is the alternating direction method of multipliers (ADMM) method (Liu et al., 2013). ADMM is an iterative algorithm very suitable for numerous convex problems and the basic idea is to update each independent variable in a proper order for each epoch until the convergence.

We first give the basic formulation of ADMM. The corresponding augmented Lagrange function of Eq. (30) is defined as:

$$\begin{aligned} \mathcal{F}_\mu(\mathcal{X}, \mathbf{Z}, \mathcal{Y}) = & \|\mathcal{X}\|_{t^*} + \frac{\lambda_1}{2} \|\tilde{\mathbf{L}}_s \mathbf{Z}^\top\|_F^2 + \frac{\lambda_2}{2} \|\Phi \mathbf{L}_\Phi \mathbf{Z}\|_F^2 \\ & + \langle \mathcal{Y}, \mathcal{X} - \mathcal{T}(\mathbf{Z}) \rangle + \frac{\mu}{2} \|\mathcal{X} - \mathcal{T}(\mathbf{Z})\|_F^2, \end{aligned} \quad (31)$$

where \mathcal{Y} is the Lagrange dual variable tensor, μ is the penalty parameter of equality constraint as well as the learning rate. Note that we do not incorporate the constraint $\mathbf{P} \odot \mathbf{Z} = \mathbf{P} \odot \mathbf{T}$ into \mathcal{F}_μ as we directly use this equality to transfer observations. Then, the ADMM alternately minimizes each of the target variable and dual variable until convergence. The iterative scheme of ADMM leads to the following updating rules:

$$\begin{cases} \mathcal{X}^{j+1} = \arg \min_{\mathcal{X}} \mathcal{F}_\mu(\mathcal{X}, \mathbf{Z}^j, \mathcal{Y}^j), \\ \mathbf{Z}^{j+1} = \arg \min_{\mathbf{Z}} \mathcal{F}_\mu(\mathcal{X}^{j+1}, \mathbf{Z}, \mathcal{Y}^j), \\ \mathcal{Y}^{j+1} = \mathcal{Y}^j + \mu (\mathcal{X}^{j+1} - \mathcal{T}(\mathbf{Z}^{j+1})). \end{cases} \quad (32)$$

For j -th iteration, we need to compute the optimal solution to each subproblem so that the ADMM guarantees the ideal solution. However, the overall computational efficiency is determined by the complexity of each subproblem and declines dramatically with the increase of problem scale.

As discussed in section 1, there exists a wealth of spatial correlations to be mined on the entire road network and integrating network-wide of data could contain more comprehensive relationships. In order to make the proposed model in Eq. (30) scalable to large network, we reformulate the ADMM scheme by improving the computation of each subproblem. Technically, we find the bottleneck (the highest time complexity) of each updating rule and accelerate it with numeric approximation methods: refining the solutions to \mathcal{X} and \mathbf{Z} subproblems using random projection and subspace iterative techniques separately. As can be found below, these useful designs make the model scalable to large-scale problems while keep high accuracy.

4.5.1. Solving \mathcal{X} subproblem with random projection

To update \mathcal{X} variable, we first arrange the first line in Eq. (32) in the standard form of t-TNN minimization:

$$\begin{aligned} \mathcal{X}^{j+1} &= \arg \min_{\mathcal{X}} \mathcal{F}_\mu(\mathcal{X}, \mathbf{Z}^j, \mathcal{Y}^j), \\ &= \arg \min_{\mathcal{X}} \|\mathcal{X}\|_{t^*} + \langle \mathcal{Y}^j, \mathcal{X} - \mathcal{T}(\mathbf{Z}^j) \rangle + \frac{\mu}{2} \|\mathcal{X} - \mathcal{T}(\mathbf{Z}^j)\|_F^2, \\ &= \arg \min_{\mathcal{X}} \|\mathcal{X}\|_{t^*} + \frac{\mu}{2} \|\mathcal{X} - (\mathcal{T}(\mathbf{Z}^j) - \mathcal{Y}^j/\mu)\|_F^2. \end{aligned} \quad (33)$$

Under the definition of t-TNN, a general choice for solving Eq. (33) is to resort to a proximity operator called tensor singular value thresholding (t-SVT). We give the result in Lemma 1 as follows.

Lemma 1. (*t-SVT (Lu et al., 2019b)*) For any tensor $\mathcal{M} \in \mathbb{R}^{n_1 \times n_2 \times n_3}$, let \mathcal{L} be any invertible linear transform and the tensor singular value decomposition (t-SVD) is given by $\mathcal{M} = \mathcal{U} *_{\mathcal{L}} \mathcal{S} *_{\mathcal{L}} \mathcal{V}^\top$, then the optimal solution to the following problem

$$\min_{\mathcal{X}} \|\mathcal{X}\|_{t^*} + \frac{\mu}{2} \|\mathcal{X} - \mathcal{M}\|_F^2,$$

is given by the t-SVT: $\mathcal{D}_{1/\mu}(\mathcal{M}) = \mathcal{U} *_{\mathcal{L}} \mathcal{S}_{1/\mu} *_{\mathcal{L}} \mathcal{V}^\top$, $\mathcal{S}_{1/\mu} = \mathcal{L}^{-1}([\mathcal{L}(\mathcal{S}) - \frac{1}{\mu}]_+)$, where $[t]_+ = \max(t, 0)$.

The variables in Lemma 1 are all in the form of tensor and this operator simply performs the soft-thresholding rule to $\mathcal{L}(\mathcal{S})$. Practically, since the t-SVD can be computed by performing matrix SVD in the transformed domain (graph spectral domain in this work), the t-SVT described above can also be calculated in an easy-to-understand fashion based on the definition of t-product (see Def. 1). Algorithm 1 summarizes the procedure to obtain $\mathcal{D}_{1/\mu}(\mathcal{M})$.

Algorithm 1: computation of t-SVT based on t-product $*_{\mathcal{L}}$

Input: $\mathcal{M} \in \mathbb{R}^{n_1 \times n_2 \times n_3}$, invertible transform \mathcal{L} , thresholding parameter $1/\mu$.

Output: $\mathcal{D}_{1/\mu}(\mathcal{M})$.

- 1 $\bar{\mathcal{M}} \leftarrow \mathcal{L}(\mathcal{M})$;
 - 2 compute each frontal slice of $\bar{\mathcal{U}}, \bar{\mathcal{S}}, \bar{\mathcal{V}}$ from the slices of $\bar{\mathcal{M}}$ by:
 - 3 **for** $i = 1$ **to** n_3 **do**
 - 4 $[\bar{\mathbf{U}}^{(i)}, \bar{\mathbf{S}}^{(i)}, \bar{\mathbf{V}}^{(i)}] \leftarrow \text{svd}(\bar{\mathbf{M}}^{(i)})$;
 - 5 $\bar{\mathbf{S}}_{1/\mu}^{(i)} \leftarrow [\bar{\mathbf{S}}^{(i)} - 1/\mu]_+$;
 - 6 $\bar{\mathbf{M}}_{1/\mu}^{(i)} \leftarrow \bar{\mathbf{U}}^{(i)} \bar{\mathbf{S}}_{1/\mu}^{(i)} \bar{\mathbf{V}}^{(i)\top}$;
 - 7 concatenate $\bar{\mathbf{M}}_{1/\mu}^{(i)}$ along the third dimension to form $\bar{\mathcal{M}}_{1/\mu}$;
 - 8 $\mathcal{D}_{1/\mu}(\mathcal{M}) \leftarrow \mathcal{L}^{-1}(\bar{\mathcal{M}}_{1/\mu})$.
-

From Lemma 1 one can see that the \mathcal{X} subproblem boils down to solve a series of matrix SVT problems on daily slices along the third axis in the transformed domain and the temporal periodicity are preserved in the TGFT tensor. This is a significant advantage of t-TNN that makes it possible to be extended to large data sets. Moreover, as daily matrices are independent on each other, the computation can be conducted in a highly-parallel way.

Despite the t-TNN itself has reduced the computation cost to some extent, there is still space for improvement. The main bottleneck of Algorithm 1 is to compute the SVD of certain $n_1 \times n_2$ matrices and the per-iteration cost is $\mathcal{O}(n_1^2 n_2 n_3)$ as discussed in section 4.1. However, tensors with sensor numbers n_2 much larger than time intervals n_1 could suffer from high computational cost at each iteration. In fact, from the calculation procedure of SVT we can observe that exact and complete SVD calculation is unnecessary for thresholding operation, because only a few singular values larger than the threshold value can have an effect. To this end, we expect to reduce the computation burden by finding an approximation of partial SVD.

A desired choice is using the random projection method to accelerate the SVD, i.e., randomized SVD (rSVD) (Halko et al., 2011). The core idea of rSVD is using a random projection matrix to help identify the subspace that dominates the pattern of matrix. Then, a rank- k approximation of the original matrix can be obtained which further leads to the approximate SVD. In general, a Gaussian i.i.d matrix can be specified as the random projection, and the subspace's orthonormal basis can be computed by the QR decomposition (Golub and Van Loan, 2013). For more details about rSVD please refer to (Halko et al., 2011).

In light of this view, we can speed up the matrix SVT calculation by the following lemma, then we adapt it for t-SVT by the property of t-product:

Lemma 2. Let $\mathbf{A} = \mathbf{Q}\mathbf{B} \in \mathbb{R}^{m \times n}$, where $\mathbf{Q} \in \mathbb{R}^{m \times k}$ is partially orthonormal, then we have:

$$\mathcal{S}_\tau(\mathbf{A}) = \mathbf{Q}\mathcal{S}_\tau(\mathbf{B}), \quad (34)$$

where $\mathcal{S}_\tau(\cdot)$ denotes the matrix SVT operator, k is the rank of \mathbf{A} .

Based on Lemma 2, we could avoid expensive computational burden by instead performing SVT on a smaller matrix $\mathbf{B} \in \mathbb{R}^{k \times n}$. If the orthonormal matrix \mathbf{Q} is available and suppose $m \geq n$, the complexity for SVD becomes $\mathcal{O}(nk^2)$, which is much cheaper than the original SVD.

To perform Lemma 2, there are two key points to carefully consider. One major challenge is how to get an appropriate \mathbf{Q} . Fortunately, the orthonormal basis can be computed from the procedure of rSVD using QR decomposition. Another task is to estimate the target rank k at each iteration of ADMM. An empirical observation is that during the training process of tensor completion, the rank increases over iterations since the missing values are filled gradually. By exploiting this prior, a simple but effective way is to set a small value at first and increase it gradually with iteration until the upper bound. Another insightful consideration of r-tSVT is that setting a small rank k in each epoch encourages the low-rank characteristics of the solution. As the threshold value $1/\mu$ decreases over iterations (to benefit convergence), a lower rank solution could improve the estimation accuracy in practice.

The whole process to get $\mathcal{D}_{1/\mu}(\tilde{\mathcal{A}})$ is summarized in Algorithm 2. Since the above lemma is based on matrix SVT, we integrate it with t-product to adapt to tensor situation. The core idea is that the computation of t-SVT can be parallelized for each slice matrix, thereby facilitating the integration of r-SVD (Zhang et al., 2018).

Algorithm 2: fast randomized t-SVT based on rSVD

Input: $\mathcal{A} \in \mathbb{R}^{n_1 \times n_2 \times n_3}$, rank parameter $k < \min\{n_1, n_2\}$, power parameter p , oversampling parameter s , transform \mathcal{L} , thresholding parameter $1/\mu$.

Output: Low rank approximation $\mathcal{D}_{1/\mu}(\tilde{\mathcal{A}})$ of $\mathcal{D}_{1/\mu}(\mathcal{A})$.

- 1 $\bar{\mathcal{A}} \leftarrow \mathcal{L}(\mathcal{A})$;
 - 2 sample a Gaussian random matrix: $\Omega \leftarrow \text{randn}(n_1, k + s)$;
 - 3 **for** $i = 1$ **to** n_3 **do**
 - 4 $\bar{\mathbf{G}} \leftarrow \bar{\mathbf{A}}^{(i)\top} \Omega$;
 - 5 conduct power iteration by:
 - 6 **for** $j = 1$ **to** p **do**
 - 7 $\bar{\mathbf{G}} \leftarrow \bar{\mathbf{A}}^{(i)\top} \bar{\mathbf{A}}^{(i)} \bar{\mathbf{G}}$;
 - 8 compute a reduced QR decomposition: $\bar{\mathbf{Q}}^{(i)} \leftarrow \text{QR}(\bar{\mathbf{G}})$;
 - 9 $\bar{\mathbf{B}}^{(i)} \leftarrow \bar{\mathbf{Q}}^{(i)\top} \bar{\mathbf{A}}^{(i)\top}$;
 - 10 concatenate $\bar{\mathbf{B}}^{(i)}$ and $\bar{\mathbf{Q}}^{(i)}$ along the third dimension to form $\bar{\mathbf{B}}, \bar{\mathbf{Q}}$ respectively;
 - 11 compute the t-SVT of $\bar{\mathbf{B}}$ using line 2-7 in Algorithm 1 to obtain $\bar{\mathbf{B}}_{1/\mu}$;
 - 12 $\bar{\mathcal{A}}_{1/\mu} \leftarrow \bar{\mathbf{Q}} *_{\mathcal{L}} \bar{\mathbf{B}}_{1/\mu}$;
 - 13 $\mathcal{D}_{1/\mu}(\tilde{\mathcal{A}}) \leftarrow \mathcal{L}^{-1}(\bar{\mathcal{A}}_{1/\mu})$.
-

There are some expositions about Algorithm 2. In our case $n_1(I) < n_2(J)$, we first transpose each slice matrix $\bar{\mathbf{A}}^{(i)}$ from $n_1 \times n_2$ to $n_2 \times n_1$ such that the resulted small matrix $\bar{\mathbf{B}}^{(i)} \in \mathbb{R}^{k \times n_1}$ requires minimal computation for SVD. Moreover, a useful technique called power iteration is applied in line 5-7 in Algorithm 2 to improve the estimation accuracy of \mathbf{Q} and Halko et al. (2011) also found that in practice $p = 1$ or 2 usually suffices.

Finally, by adopting Algorithm 2, the optimal solution to update \mathcal{X} in Eq. (33) is:

$$\mathcal{X}^{j+1} = \mathcal{D}_{1/\mu}(\mathcal{T}(\mathbf{Z}^j) - \mathcal{Y}^j/\mu). \quad (35)$$

4.5.2. Solving \mathbf{Z} subproblem with conjugate gradient

The second term in Eq. (32) is the optimization of spatial proximity and temporal continuity regularization that closely related to kriging tasks. After introducing the (inverse) tensorization operator $\mathbf{Z} = \mathcal{T}^{-1}(\mathcal{X})$, we can update \mathbf{Z} in the form of matrix easily:

$$\begin{aligned} \mathbf{Z}^{j+1} &= \arg \min_{\mathbf{Z}} \mathcal{F}_{\mu}(\mathcal{X}^{j+1}, \mathbf{Z}, \mathcal{Y}^j), \\ &= \arg \min_{\mathbf{Z}} \frac{\lambda_1}{2} \|\tilde{\mathbf{L}}_s \mathbf{Z}^{\top}\|_F^2 + \frac{\lambda_2}{2} \|\Phi \mathbf{L}_{\Phi} \mathbf{Z}\|_F^2 + \langle \mathcal{Y}^j, \mathcal{X}^{j+1} - \mathcal{T}(\mathbf{Z}) \rangle + \frac{\mu}{2} \|\mathcal{X}^{j+1} - \mathcal{T}(\mathbf{Z})\|_F^2, \\ &= \arg \min_{\mathbf{Z}} \underbrace{\frac{\lambda_1}{2} \|\tilde{\mathbf{L}}_s \mathbf{Z}^{\top}\|_F^2 + \frac{\lambda_2}{2} \|\Phi \mathbf{L}_{\Phi} \mathbf{Z}\|_F^2 + \frac{\mu}{2} \|\mathbf{Z} - \mathcal{T}^{-1}(\mathcal{X}^{j+1} + \mathcal{Y}^j/\mu)\|_F^2}_{\mathcal{H}(\mathbf{Z})}. \end{aligned} \quad (36)$$

Set the gradient of $\mathcal{H}(\mathbf{Z})$ to zero, we can have the least square solution:

$$\lambda_1 \tilde{\mathbf{L}}_s^{\top} \tilde{\mathbf{L}}_s + \lambda_2 (\Phi \mathbf{L}_{\Phi})^{\top} \Phi \mathbf{L}_{\Phi} \mathbf{Z} + \mu \mathbf{Z} = \mu \mathcal{T}^{-1}(\mathcal{X}^{j+1} + \mathcal{Y}^j/\mu). \quad (37)$$

Eq. (37) is a standard Sylvester matrix equation in the form of $\mathbf{A}\mathbf{X} + \mathbf{X}\mathbf{B} = \mathbf{C}$. Typically, a direct manner to solve this system is vectorizing it into a standard linear equations, as shown in Eq. (38).

$$(\lambda_1 \tilde{\mathbf{L}}_s^{\top} \tilde{\mathbf{L}}_s \otimes \mathbf{I}_{JK} + \lambda_2 \mathbf{I}_J \otimes \mathbf{L}_{\Phi}^{\top} \Phi^{\top} \Phi \mathbf{L}_{\Phi} + \mu \mathbf{I}_{JK}) \text{vec}(\mathbf{Z}) = \mu \text{vec}(\mathcal{T}^{-1}(\mathcal{X}^{j+1} + \mathcal{Y}^j/\mu)), \quad (38)$$

where \otimes is the Kronecker product, $\text{vec}(\cdot)$ denotes the vectorization operator, and \mathbf{I}_n denotes an identity matrix of size $n \times n$. This conversion holds due to the fact that $\text{vec}(\mathbf{A}\mathbf{X}\mathbf{B}) = (\mathbf{B}^{\top} \otimes \mathbf{A}) \text{vec}(\mathbf{X})$.

However, the computational complexity of this vectorized solution is $\mathcal{O}(I^3 J^3 K^3)$, which is both computationally expensive and memory-consuming for large-scale problems. An alternative solution for Sylvester system is using Bartels-Stewart method (Golub and Van Loan, 2013). Although the cost can be reduced to $\mathcal{O}(I^3 K^3 + J^3)$, it is still prohibitive in practice. Note that in our case \mathbf{A} and \mathbf{B} are highly structured, i.e., symmetric and positive definite, so that the matrix vector multiplies involving them can be efficient. Taking this into account, subspace iterative methods could potentially perform better for fixing this problem.

Conjugate gradient (CG) is a representative Krylov subspace iteration method and has been verified to be an efficient and stable manner in recent works (Kalofolias et al., 2014; Rao et al., 2015). One distinct advantage of CG is that it is nonparametric and requires only a small number of iterations to solve the structured linear system with desired accuracy. By using the vectorization operation in Eq. (38), we apply CG to such a symmetric positive definite system to approximate its numeric solution. Details about CG is omitted for simplicity and we present the procedure for solving \mathbf{Z} variable in Algorithm 3.

Algorithm 3: Conjugate gradient for \mathbf{Z} -subproblem

Input: $\mathbf{Z} \in \mathbb{R}^{(IK) \times J}$, $\mathcal{X}, \mathcal{Y}, \mu, \mathbf{L}_s, \mathbf{E}_n, \lambda_1, \lambda_2$, maximum iterations t .

Output: Estimated variable $\hat{\mathbf{Z}}$.

```
1  $\mathcal{V}(\mathbf{Z}) \leftarrow (\lambda_1 \tilde{\mathbf{L}}_s^T \tilde{\mathbf{L}}_s \otimes \mathbf{I}_{IK} + \lambda_2 \mathbf{I}_J \otimes \mathbf{L}_\Phi^T \Phi^T \Phi \mathbf{L}_\Phi + \mu \mathbf{I}_{IJK}) \text{vec}(\mathbf{Z});$ 
2  $\mathbf{r}_0 \leftarrow \mu \text{vec}(\mathcal{T}^{-1}(\mathcal{X}^{j+1} + \mathcal{Y}^j / \mu)) - \mathcal{V}(\mathbf{Z});$ 
3  $\mathbf{q}_0 \leftarrow \mathbf{r}_0;$ 
4 for  $i = 1$  to  $t$  do
5    $\mathbf{Q}_i \leftarrow \text{reshape}(\mathbf{q}_i);$ 
6    $\alpha_i \leftarrow \mathbf{r}_i^T \mathbf{r}_i / (\mathbf{q}_i^T \mathcal{V}(\mathbf{Q}_i));$ 
7    $\mathbf{z}_{i+1} \leftarrow \mathbf{z}_i + \alpha_i \mathbf{q}_i;$ 
8    $\mathbf{r}_{i+1} \leftarrow \mathbf{r}_i - \alpha_i \mathcal{V}(\mathbf{Q}_i);$ 
9    $\beta_i \leftarrow \frac{\mathbf{r}_{i+1}^T \mathbf{r}_{i+1}}{\mathbf{r}_i^T \mathbf{r}_i};$ 
10   $\mathbf{q}_{i+1} \leftarrow \mathbf{r}_{i+1} + \beta_i \mathbf{q}_i;$ 
11  $\hat{\mathbf{Z}} \leftarrow \text{reshape}(\mathbf{z}_t).$ 
```

In Algorithm 3, each iteration only involves one single matrix-vector product, several inner products and scalar operations. This makes it highly scalable to large problems and we can incorporate it in the ADMM framework.

The main cost of Algorithm 3 is the matrix-vector product to calculate $\mathcal{V}(\mathbf{Q}_i)$ and the time complexity is $\mathcal{O}(I^2 J^2 K^2)$ for each inner CG iteration. What is noteworthy is that this cost can be further reduced if we first compute the matrix-matrix products in $\lambda_1 \mathbf{Q}_i \tilde{\mathbf{L}}_s^T \tilde{\mathbf{L}}_s + (\lambda_2 \mathbf{L}_\Phi^T \Phi^T \Phi \mathbf{L}_\Phi + \mu \mathbf{I}) \mathbf{Q}_i$ and then obtain $\mathcal{V}(\mathbf{Q}_i)$ using $\text{reshape}(\cdot)$ directly. And the complexity is essentially $\mathcal{O}(IJK(IK + J))$ in this case, which is substantially reduced compared to $\mathcal{O}(I^3 J^3 K^3)$ required by the vectorized solution.

4.5.3. Solution algorithm

Having solved each ADMM subproblem, the proposed LETC algorithm is finally summarized in Algorithm 4. In this implementation, the updating order follows $\{\mathcal{X}^j \Rightarrow \mathbf{Z}^j \Rightarrow \mathcal{Y}^j\}$ and the estimated data values can be returned either in matrix $\hat{\mathbf{Z}}$ or in tensor $\hat{\mathcal{X}}$. In line 8, we increase the penalty parameter as well as the learning rate μ to promote the convergence of ADMM, and also increase the target rank k for Algorithm 2. As we solve both of the two subproblems in a highly scalable routine, this algorithm is efficient for large-scale kriging tasks. Moreover, two most important hyper-parameters in Algorithm 4 are the regularization parameters λ_1, λ_2 . These coefficients function as a balance between t-TNN minimization and local consistency penalty, and we will discuss the impacts of them in Section 5.3.3.

Algorithm 4: Spatiotemporal Laplacian enhanced low-rank tensor completion for kriging

Input: Measured speed matrix \mathbf{T} , indicating matrix \mathbf{P} , linear transform \mathcal{L} , learning rate μ , initial rank parameter k , regularization terms and coefficients $\mathbf{L}_s, \mathbf{E}_n, \lambda_1, \lambda_2$, convergence condition ϵ .

Output: Estimated full matrix $\hat{\mathbf{Z}}$.

```
1 Initialize  $\mathcal{Y}^0$  as zeros, and set  $\mathbf{P} \odot \mathbf{Z}^0 \leftarrow \mathbf{P} \odot \mathbf{T}, j \leftarrow 0;$ 
2 while not converged do
3   Update  $\mathcal{X}^{j+1}$  by Eq. (35) and Algorithm 1, 2;
4   Update  $\mathbf{Z}^{j+1}$  by Algorithm 3;
5   Transmit the observations by setting  $\mathbf{P} \odot \mathbf{Z}^{j+1} \leftarrow \mathbf{P} \odot \mathbf{T};$ 
6   Update  $\mathcal{Y}^{j+1}$  by  $\mathcal{Y}^{j+1} \leftarrow \mathcal{Y}^j + \mu (\mathcal{X}^{j+1} - \mathcal{T}(\mathbf{Z}^{j+1}));$ 
7    $e^{j+1} \leftarrow \|\mathbf{Z}^{j+1} - \mathbf{Z}^j\|_F / \|\mathbf{Z}^j\|_F;$ 
8   Increase the learning rate  $\mu$  and rank parameter  $k$  with a fixed step;
9   if  $e^{j+1} < \epsilon$  then
10  | Converge.
11  |  $j \leftarrow j + 1;$ 
```

4.6. Overall computational complexity analysis

The computational complexity of each solving step is introduced separately and we give a brief summary and discussion here. Overall, the main cost of Algorithm 4 is t-SVT in \mathcal{X} -subproblem and CG in \mathbf{Z} -subproblem. The step-by-step computational complexity of Algorithm 2 and 3 is summarized in Tab. 1 and Tab. 2, respectively. Since lines 4-11 in Tab. 1 are conducted for each daily slice, their complexity become K times. As we can see, the main bottleneck of LETC is the matrix-vector product in CG iteration. But this implementation is efficient enough for large-scale applications.

Table 1: Time complexity analysis for Algorithm 2.

Line No.	Specific operation	Complexity
4	$\bar{\mathbf{G}} \leftarrow \bar{\mathbf{A}}^{(i)\top} \mathbf{\Omega}$	$\mathcal{O}(kJJ)$
7	$\bar{\mathbf{G}} \leftarrow \bar{\mathbf{A}}^{(i)\top} \bar{\mathbf{A}}^{(i)} \bar{\mathbf{G}}$	$\mathcal{O}(kJJ)$
8	$\bar{\mathbf{Q}}^{(i)} \leftarrow \text{QR}(\bar{\mathbf{G}})$	$\mathcal{O}(Jk^2)$
9	$\bar{\mathbf{B}}^{(i)} \leftarrow \bar{\mathbf{Q}}^{(i)\top} \bar{\mathbf{A}}^{(i)\top}$	$\mathcal{O}(kJJ)$
11	$\text{svd}(\bar{\mathbf{B}}^{(i)})$	$\mathcal{O}(Ik^2)$
12	$\bar{\mathbf{A}}_{1/\mu} \leftarrow \bar{\mathbf{Q}} *_{\mathcal{L}} \bar{\mathbf{B}}_{1/\mu}$	$\mathcal{O}(kJJK)$

Table 2: Time complexity analysis for Algorithm 3.

Line No.	Specific operation	Complexity
1	Compute $\mathcal{V}(\mathbf{Z})$	$\mathcal{O}(IJK(J + IK))$
2	Compute \mathbf{r}_0	$\mathcal{O}(IJK)$
6	$\alpha_i \leftarrow \mathbf{r}_i^\top \mathbf{r}_i / (\mathbf{q}_i^\top \mathcal{V}(\mathbf{Q}_i))$	$\mathcal{O}(IJK(J + IK))$
7,8,10	Compute $\mathbf{z}_{i+1}, \mathbf{r}_{i+1}, \mathbf{q}_{i+1}$	$\mathcal{O}(IJK)$
11	$\beta_i \leftarrow \mathbf{r}_{i+1}^\top \mathbf{r}_{i+1} / (\mathbf{r}_i^\top \mathbf{r}_i)$	$\mathcal{O}(IJK)$

5. Case study

In this section, we conduct experiments to evaluate the kriging performance of the proposed LETC model on two real-world and network-wide traffic speed datasets under different settings. First we briefly describe the datasets and introduce some state-of-the-art kriging baseline models. Apart from model comparison, we also conduct various ablation studies and sensitivity studies for algorithmic analysis. All the experiments are carried out on a Windows 10 platform with Intel(R) Core(TM) i7-12700KF 3.60GHz CPU (12 cores in total) and 32 GB RAM. **The NumPy implementation is shared in our GitHub repository: <https://github.com/tongnie/tensor4kriging>.**

5.1. Data preparation and experiment setup

5.1.1. Spatiotemporal traffic speed datasets

As we aim to evaluate kriging performances on large data, two publicly available large-scale traffic speed datasets: PeMS-4W freeway speed data (Chen et al., 2021a) and Portland highway speed data are used for benchmark experiments. These datasets are briefly summarized as follows:

- **PeMS-4W freeway loop speed data¹**: Large-scale traffic speed data collected from 11160 loop sensors installed on the freeway in California. The speed records include the first 4 weeks in 2018 with a 5-min resolution and it can be organized in a spatiotemporal matrix of shape (8064×11160) or a tensor of shape $(288 \times 11160 \times 28)$. This data set also provides a travel distance based adjacent matrix. This data contains about 90 million observations.
- **Portland highway loop speed data²**: The Portland database provides 20-second granularity loop detector records from freeways in the Portland-Vancouver metropolitan region. We collect traffic speed data from 1057 loop sensors with a 15-minute resolution over 3 months (from January 1 to March 31, 2021). The data size is (8640×1057) in matrix or $(96 \times 1057 \times 90)$ in tensor. This data provides the location information of all sensors. This data contains about 10 million observations.

The input data is arranged in a third-order tensor of (time of day \times locations \times days) or a matrix of (time points \times locations). One can find that the 'location' dimension is much larger than the 'time of day' dimension for both of the two datasets. Different from other large datasets used for traffic prediction studies, which usually feature a large 'days' dimension, the two data with pretty large 'locations' dimension are more suitable for testing the extendability of kriging models.

5.1.2. Competing models and experiment settings

In order to demonstrate the superiority of the proposed model, we compare LETC with several state-of-the-art baseline methods. These baselines not only contain typical tensor/matrix based spatiotemporal kriging models, but also cover advanced methods from machine learning communities.

- **TGMF (Zhang et al., 2020)**: Temporal geometric matrix factorization. This model uses graph Laplacian and one-order Toeplitz matrix as spatial and temporal regularization. ADMM is used to update variables.
- **LSTM-GRMF (Yang et al., 2021)**: This model extends the graph Laplacian regularized matrix factorization framework with LSTM temporal regularization. It can perform online imputation and prediction, while we only test the performance of static training and kriging phase.
- **FMDT-Tucker (Yamamoto et al., 2022)**: Fast algorithm for multi-way delay embedded (MDT, aka., Hankelization) Tucker decomposition. This work is an enhanced version of Yokota et al. (2018) where the MDT is accelerated by FFT. It utilizes the shift-invariant features of rows/columns to perform image-inpainting which can also achieve spatiotemporal kriging.

¹from <https://doi.org/10.5281/zenodo.3939793>.

²from <https://portal.its.pdx.edu/home>.

- **GLTL (Bahadori et al., 2014)**: Greedy low-rank tensor learning. This is a classical tensor learning method for spatiotemporal kriging and is solved by greedy algorithm.
- **KPMF (Zhou et al., 2012)**: Kernelized probabilistic matrix factorization. Row-wise and column-wise kernel(covariance) functions are used as graph side information and a Gaussian process prior is imposed on the factor matrices. This model is solved by stochastic gradient descend method.
- **GLOSS (Sofuoglu and Aviyente, 2022)**: Graph regularized low-rank plus temporally smooth sparse decomposition model, which uses the unfolding-based nuclear norm (Liu et al., 2013) to capture low-rankness. One-order Toeplitz and symmetric graph Laplacian are also adopted for local smoothness.
- **WDG-CP (Li et al., 2020)**: Weakly-dependent graph regularized CANDECOMP/PARAFAC (CP) tensor decomposition. A L_1 norm penalty is adopted to encourage sparsity of temporal factor.
- **LETC-separate**: We also examine a variation of our LETC model that handles the global (low-rank) and local (spatially and temporally regularized) parts separately. In this setting, we first conduct imputation for missing data points by keeping the missing rows/columns excluded, using only the first term in Eq. (30). Then we conduct kriging on the imputed matrix using only the last two terms.

In fact, although FMDT-Tucker, GRALS and KPMF are not designed for spatiotemporal kriging in their original works (image inpainting and collaborative filtering), the intrinsic mathematical problems are the same as ours such that they can be transferred to this task. Moreover, BKMF (Lei et al., 2022) and GNNs (Wu et al., 2021a; Liang et al., 2022) are also emerging kriging methods, but we do not include them in the baselines because the Bayesian hyper-parameter sampling procedure in former is time-consuming and the training stage in latter also brings heavy computational burden and memory consumption. Both of them are not well-suited for large-scale problems.

To evaluate the models' performance, a series of observation conditions are tested: we randomly mask the ground truth values of 30%, 50%, 70% locations as unmeasured locations (without sensors), and select 20%, 50% time intervals as unmeasured time (non-operational time). So there are six test scenarios in total, and we name them SM3TM2, SM5TM2, SM7TM2, SM3TM5, SM5TM5, SM7TM5, respectively. Furthermore, we also add 20% randomly element-wise missing data to simulate the reality. The performances are evaluated by comparing the estimated values with masked ones. Two evaluation metrics are used in this section: mean absolute error (MAE) and root mean square error (RMSE):

$$\begin{aligned} \text{MAE} &= \frac{1}{|\Omega_m|} \sum_{i \in \Omega_m} |x_i - \hat{x}_i|, \\ \text{RMSE} &= \sqrt{\frac{1}{|\Omega_m|} \sum_{i \in \Omega_m} (x_i - \hat{x}_i)^2}, \end{aligned} \tag{39}$$

where $\Omega_m = \{(i, j, k) \mid \text{when } x_{ijk} \text{ is manually masked and observed data in original tensor}\}$. Detailed hyper-parameter settings for LETC and other baselines are given in [Appendix A](#).

5.2. Network-wide kriging results analysis and model comparison

The comparison of kriging performances of LETC and its competing baselines are given in Tab. 3. All experiments are repeated 5 times with 5 random seeds to generate missing nodes, and the mean values as well as standard deviations are reported. We also report the CPU running time of all models on PeMS data in Tab. 4, to show the computation cost. To focus on the basic performance of LETC and reduce the number of hyper-parameters to be discussed, we only display the results of setting $h(\tilde{\mathbf{A}}_s) = \tilde{\mathbf{A}}_s$ in Eq. (19) and $\omega_1 = \omega_2 = \omega_T = 1$ in Eq. (12). More superior performances of LETC can be achieved by carefully selecting more expressive diffusion kernels in section 4.3 as well as temporal weights in section 4.1 and tuning these hyper-parameters.

As can be seen that LETC achieves the best kriging results consistently in all testing scenarios. By setting different τ values, LETC can adapt to various temporal perceptual fields. With the decrease of both spatial and temporal observation rates, the performances of all models are degenerated while LETC is supposed to be more robust. Compared with performing imputation and kriging separately, the holistic LETC always achieves better results. This finding demonstrates the importance of modeling global and local correlations at the same time. On the one hand, local smoothness benefits low-rank tensor completion by acting as physical constraints. On the other hand, global information existing beyond local proximity provides more referable features for neighbor nodes to avoid over-smoothing. Therefore, LETC can achieve network-wide kriging with high accuracy, even though there exists a large proportion of incomplete observations (missing data) in measured locations.

Observing the running time in Tab. 4, we can find another superiority of LETC is that it can save nearly half the time cost compared to WDG-CP, which is the most scalable method in the baselines. As discussed in Section 4.6, the computational bottleneck is the updating of graph regularization terms which would introduce

Table 3: Kriging evaluation results on PeMS-4W and Portland data

Models	PeMS-4W (MAE/RMSE)					
	SM0.3,TM0.2	SM0.5,TM0.2	SM0.7,TM0.2	SM0.3,TM0.5	SM0.5,TM0.5	SM0.7,TM0.5
TGMF	4.48±0.02/7.46±0.04	4.59±0.01/7.60±0.04	4.75±0.00/7.90±0.03	5.15±0.01/8.44±0.03	6.16±0.03/9.17±0.05	6.35±0.01/9.55±0.03
LSTM-GRMF	2.73±0.05/5.27±0.06	3.25±0.03/6.07±0.06	3.68±0.04/6.89±0.06	2.76±0.02/5.29±0.03	3.39±0.02/6.08±0.04	3.84±0.02/6.92±0.04
FMDT-Tucker	3.07±0.08/5.58±0.12	3.29±0.06/5.92±0.08	3.84±0.02/6.97±0.08	3.49±0.05/5.98±0.10	3.61±0.01/6.50±0.05	3.95±0.05/7.37±0.08
GLTL	5.98±0.28/9.12±0.41	6.10±0.21/9.33±0.33	6.40±0.15/9.86±0.26	6.06±0.11/9.44±0.18	6.28±0.19/9.80±0.40	6.33±0.15/9.98±0.31
KPMF	4.43±0.06/7.66±0.08	5.08±0.04/8.40±0.10	6.45±0.11/9.61±0.19	5.19±0.08/8.44±0.26	6.57±0.10/9.34±0.42	6.88±0.12/9.74±0.36
WDG-CP	3.10±0.00/5.66±0.03	3.54±0.01/6.31±0.02	4.35±0.00/7.32±0.02	3.27±0.00/5.89±0.02	3.99±0.01/6.88±0.04	4.64±0.02/7.66±0.02
GLOSS	3.92±0.02/7.00±0.04	4.35±0.03/7.95±0.02	5.16±0.03/9.02±0.02	4.93±0.00/8.57±0.03	5.66±0.02/8.75±0.05	6.91±0.04/9.62±0.10
LETC-separate	2.72±0.00/5.02±0.03	3.16±0.02/5.69±0.03	3.76±0.00/6.65±0.03	3.07±0.01/5.60±0.04	3.44±0.03/6.12±0.03	3.79±0.02/6.71±0.04
LETC($\tau = 1$)	2.48±0.01/4.82±0.02	3.07±0.01/5.68±0.04	3.62±0.02/6.46±0.04	2.58±0.01/5.06±0.03	3.16±0.00/5.79±0.03	3.64±0.00/6.49±0.02
LETC($\tau = 2$)	2.45±0.01/4.84±0.03	3.06±0.01/5.64±0.02	3.63±0.01/6.47±0.02	2.65±0.01/5.19±0.04	3.18±0.00/5.85±0.04	3.63±0.03/6.48±0.03
LETC($\tau = 3$)	2.53±0.03/5.07±0.05	3.13±0.02/5.83±0.03	3.64±0.01/6.55±0.02	2.80±0.01/5.51±0.02	3.30±0.01/6.11±0.02	3.69±0.01/6.62±0.03

Models	Portland (MAE/RMSE)					
	SM0.3,TM0.2	SM0.5,TM0.2	SM0.7,TM0.2	SM0.3,TM0.5	SM0.5,TM0.5	SM0.7,TM0.5
TGMF	5.56±0.04/8.52±0.07	6.21±0.03/8.90±0.07	7.23±0.02/9.53±0.05	5.79±0.02/8.76±0.03	6.38±0.01/9.10±0.03	7.48±0.02/11.42±0.04
LSTM-GRMF	3.95±0.03/6.83±0.06	4.55±0.02/7.39±0.04	5.57±0.01/8.61±0.03	4.10±0.02/7.08±0.05	4.74±0.04/7.44±0.06	5.50±0.02/8.46±0.03
FMDT-Tucker	6.54±0.01/9.79±0.01	6.65±0.05/9.72±0.09	6.84±0.05/10.06±0.09	6.59±0.04/9.83±0.10	6.66±0.03/9.65±0.07	6.85±0.03/10.11±0.05
GLTL	7.57±0.21/10.22±0.31	7.77±0.24/10.85±0.50	9.32±0.33/12.55±0.48	8.40±0.22/11.16±0.41	9.83±0.19/13.15±0.37	10.89±0.28/14.99±0.46
KPMF	5.78±0.04/9.06±0.08	6.12±0.04/8.91±0.07	7.75±0.03/10.55±0.07	4.35±0.05/7.35±0.10	6.52±0.04/9.41±0.07	6.65±0.04/9.89±0.06
WDG-CP	3.84±0.00/6.98±0.01	4.54±0.01/7.29±0.03	5.47±0.02/8.33±0.04	4.31±0.00/7.28±0.02	4.96±0.01/7.77±0.02	5.76±0.01/8.96±0.03
GLOSS	4.90±0.03/7.95±0.07	5.80±0.03/8.97±0.06	6.82±0.04/10.26±0.08	5.28±0.04/8.37±0.06	5.54±0.03/8.67±0.05	7.05±0.03/10.53±0.06
LETC-separate	4.08±0.01/6.91±0.02	4.84±0.01/7.41±0.01	5.47±0.00/8.32±0.02	5.01±0.02/8.09±0.01	5.37±0.01/7.97±0.01	5.83±0.01/8.67±0.02
LETC($\tau = 1$)	3.78±0.02/6.74±0.02	4.44±0.01/7.14±0.02	5.35±0.00/8.33±0.02	3.96±0.03/6.87±0.02	4.67±0.01/7.35±0.02	5.44±0.00/8.38±0.02
LETC($\tau = 2$)	3.78±0.00/6.70±0.01	4.45±0.00/7.21±0.02	5.34±0.01/8.29±0.03	4.13±0.01/7.29±0.02	4.70±0.00/7.46±0.01	5.54±0.01/8.57±0.02
LETC($\tau = 3$)	3.84±0.01/6.92±0.01	4.45±0.00/7.23±0.02	5.39±0.00/8.42±0.02	4.33±0.01/7.62±0.01	4.86±0.00/7.73±0.01	5.76±0.01/8.91±0.02

Best results are bold marked.

Table 4: Running time on PeMS-4W data

Models	PeMS-4W,running time(in second)					
	SM0.3,TM0.2	SM0.5,TM0.2	SM0.7,TM0.2	SM0.3,TM0.5	SM0.5,TM0.5	SM0.7,TM0.5
TGMF	2511.6	2594.5	2739.2	2727.3	2795.1	2844.1
LSTM-GRMF	8965.7	8465.3	8382.2	8172.3	8437.1	8715.3
FMDT-Tucker	2892.8	9311.1	5783.6	4925.3	10902.1	6353.0
GLTL	7408.5	7808.0	6522.9	9673.7	6652.5	6118.5
KPMF	3488.1	1418.4	824.7	2343.9	4918.2	3763.3
WDG-CP	1979.5	2057.7	2056.6	2049.3	2045.9	2214.5
GLOSS	6390.8	6384.9	6350.8	6333.8	6372.5	6342.1
LETC	990.6	1075.1	1084.3	1067.9	1152.5	1164.3

Best results are bold marked.

large matrix equations, so the room for improvement is limited. Note that KPMF adopts stochastic gradient descent method to update parameters, which is susceptible to local minima, so it could converge to a inferior solution with fewer iteration times. LSTM-GRMF also produces competitive performances, especially when TM missing rate is high. Owing to the elaborate LSTM model, it can learn long-term temporal dependency and more complex trends in time series from training data, to produce reasonable estimates when less temporal data is given. However, the costs are a lot of training expenses and memory consumption, which are not suitable for network-wide applications. Moreover, both CP, Tucker and MF based models in the baselines require an accurate rank estimation in advance and this parameter has great impacts on estimation accuracy and convergence. Although Algorithm 2 also contains a rank parameter, in later paragraphs we show that the rank in rSVD has minimal impact on accuracy. Overall, the proposed LETC achieves state-of-the-art performances in all evaluating tasks, while requires the least computational burden at the same time.

Furthermore, we give some kriging results on both two data sets in Fig. 6 and 7 to intuitively show the speed estimation performances. Each figure depicts the estimation value and ground truth value for roads randomly selected from unmeasured locations. Overall, LETC estimates accurate time series for unknown locations, even with low observation rate as well as temporal loss. Another facet can be found that LETC produces relatively more smooth and denoised signals than the raw data due to the temporal regularization and low-rank condition.

We also give the results of half a day on the first day of PeMS data for detailed comparison in Fig. 8. As can be seen, LETC produces more smooth and stable time series than TGMF and LSTM-GRMF. With the elimination of data noises, LETC estimation is closer to the ground truth value. Because there is totally no historical data available, the LSTM model which is widely used to perform time-dimension prediction, is less effective and fluctuates a lot.

The ground truth speed values, LETC and LSTM-GRMF kriging speed values as well as the estimation residuals (absolute value of the difference between the true value and the estimated value) of LETC are visualized on the whole California highway network in Fig. 9 (more examples are given in Appendix B). Moreover, we also

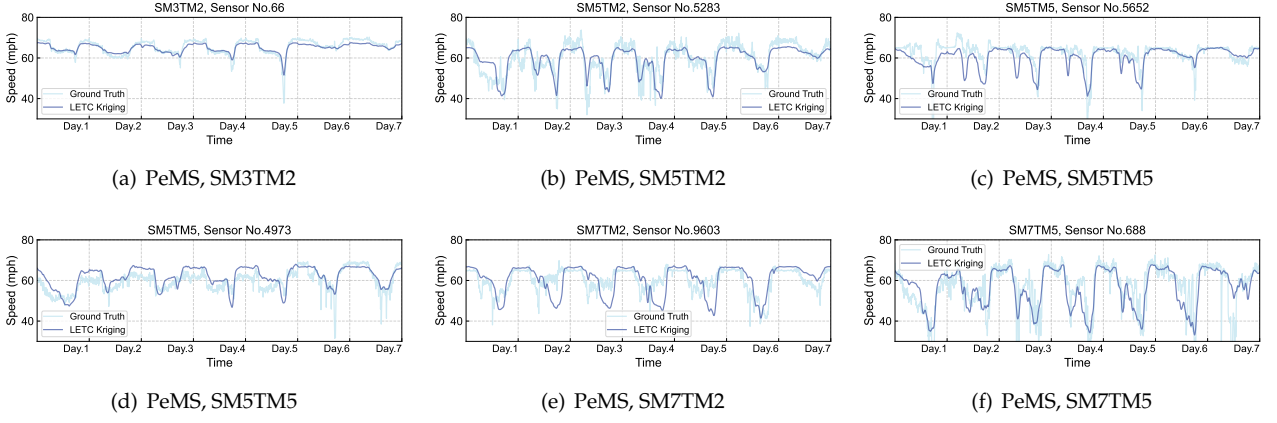


Figure 6: Kriging results visualization for PeMS-4W data. Six randomly selected sensors with different observation conditions are shown. The ground truth values and estimation values are given for comparison.

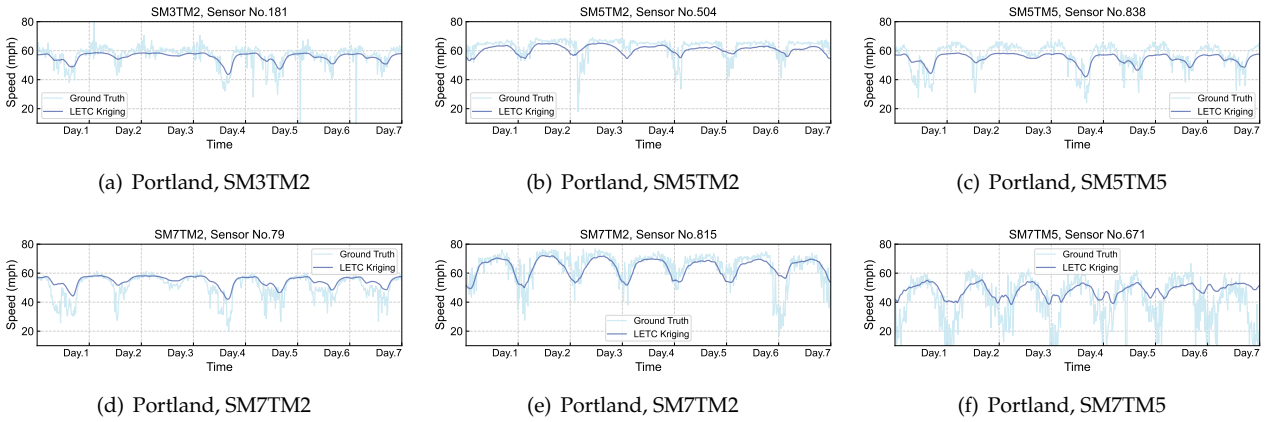


Figure 7: Kriging results visualization for Portland data. Six randomly selected sensors with different observation conditions are shown. The ground truth values and estimation values are given for comparison.

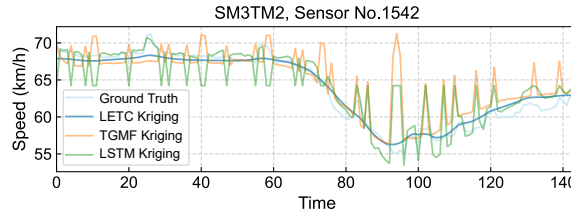


Figure 8: Detailed comparison of different kriging models.

display the Weighted Mean Absolute Percentage Error (WMAPE) of each sensor in Fig. 10.

As we can see, LETC can capture not only the global spatial distributions of traffic speed, but also the speed changes due to local congestion of morning peak. Compared (a), (b) with (d), LETC produces more realistic speed patterns than LSTM-GRMF, which is the best model in the baselines, especially for the local speed changes in congestion areas. Fig. 9 (c) also shows the LETC estimated and true speed values fit well, with more than 90% of road segments whose residual values are less than 5. The kriging errors of each link in Fig. 10 (a) demonstrate that relatively big errors occur in the areas where there is few or even no neighbor sensors, or congestion districts (e.g., south Bay area) with drastic changes in traffic speed. As kriging is in fact to aggregate the data of neighbor sensors, the estimation difficulty increases when little referable information is available. Overall, LETC produces smaller sensor-level errors than benchmark model on average, especially for those sensors located at congestion areas.

5.3. Algorithmic analysis

5.3.1. Ablation studies

To inspect the significance of each component of the proposed model, in this part we conduct ablation studies to compare the performances of several model variations. These variations include three aspects: accelerating

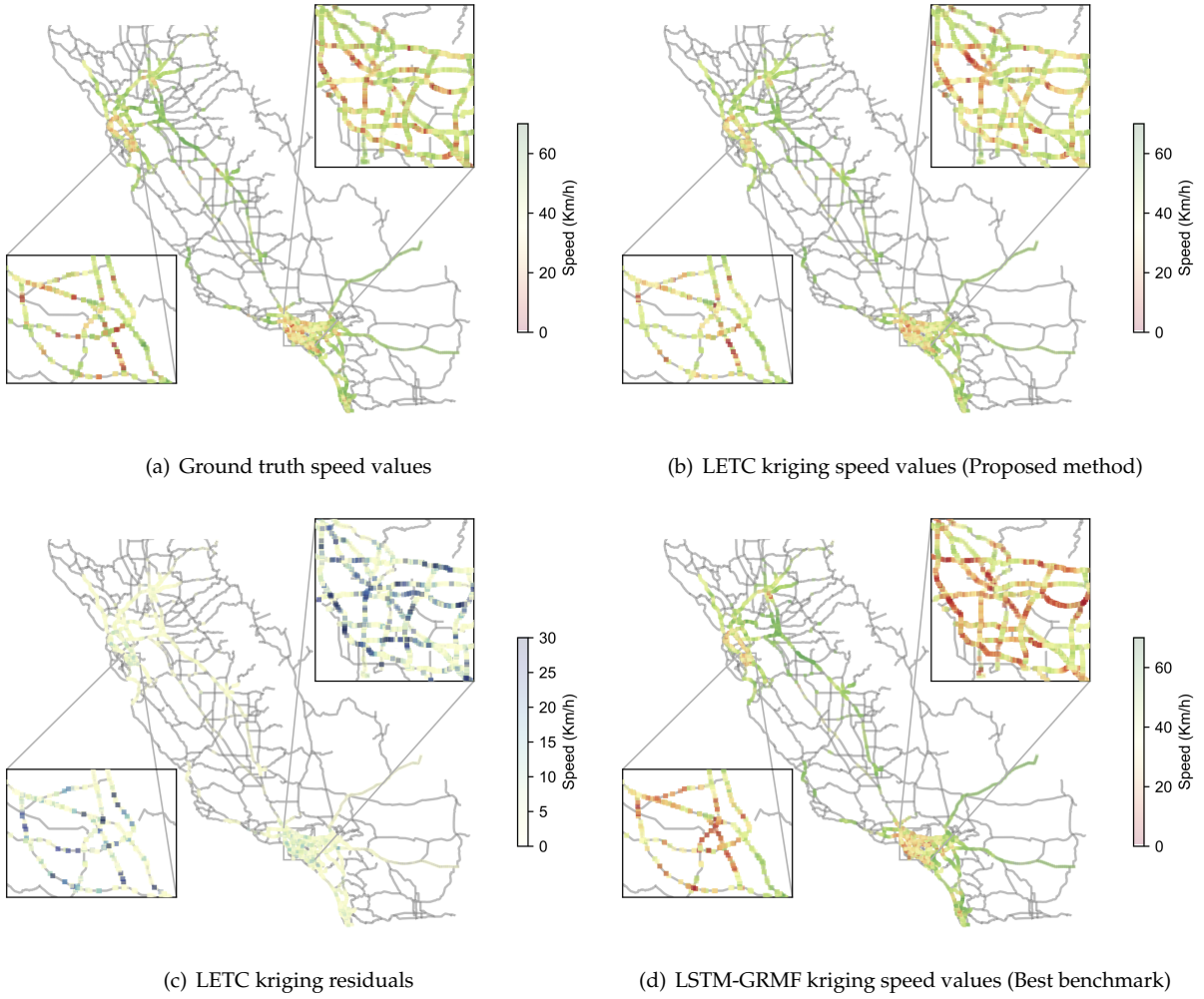


Figure 9: LETC kriging results on the PeMS highway network. Traffic state at 7:00 in the morning is displayed as an example. (a) Ground truth values. (b) LETC estimated traffic speed values. (c) LETC kriging residuals of each sensor. (d) LSTM-GRMF estimated traffic speed values.

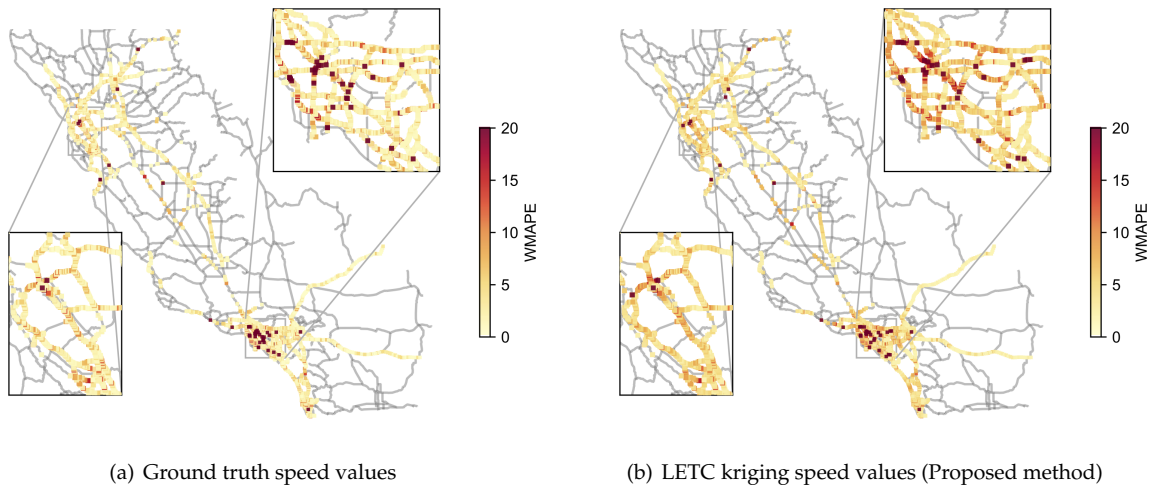


Figure 10: WMAPE of each sensor on the PeMS highway network. (a) WMAPE of LETC. (b) WMAPE of LSTM-GRMF.

algorithms, tensor nuclear norm, and spatiotemporal regularization.

Ablation studies about accelerating algorithms:

- **LETC-CG iter3** and **LETC-CG iter10**: To test the impact of the numbers of CG inner loops, we set 3 and 10 iterations for implementing Algorithm 3.

- **LETC-nCG**: LETC without conjugate gradient. The matrix equation in Eq. (37) is solved by using the Bartels-Stewart method and this algorithm is achieved by directly calling a package API function `scipy.linalg.solve_sylvester()`.
- **LETC-nRSVD**: LETC without randomized SVD. The economic (compact) SVD is used instead.

Ablation studies about unitary transform and TNN:

- **LETC-FFT**: We replace TGFT with traditional FFT, then the t-TNN becomes the previously developed tensor nuclear norm (Lu et al., 2019a).
- **LETC-GFT**: We replace the TGFT in our model by the original GFT used in (Deng et al., 2021). To achieve this adjustment, we first transpose the input tensor into shape of (time of day \times days \times locations) and calculate the graph operator in Eq. (10) by spatial Laplacian. Then, the GFT is performed on the 'location' mode.
- **LETC-ROM**: Perform unitary transform by constructing random orthogonal matrix (Lu et al., 2019b).
- **LETC-SVD**: Perform unitary transform by computing the SVD of mode-3 unfolding (Chen et al., 2021a).
- **LETC-SNN**: We replace t-TNN by sum of nuclear norm (SNN), which is another widely used tensor norm definition developed by (Liu et al., 2013).

Ablation studies about spatial and temporal dependency regularization:

- **LETC-circulant**: LETC with circulant and undirected temporal Laplacian by setting $\mathbf{L}'_{\Phi} = \mathbf{L}_{\Phi}\mathbf{L}_{\Phi}^T$ and $\Phi = \mathbf{I}_T$.
- **LETC-symmetric**: LETC with symmetric graph Laplacian regularization, which is commonly used for spatial modeling.

Table 5: Ablation studies

Models	Portland	
	MAE/RMSE	Running time (in second)
LETC(CG iter3)	4.61/7.40	145.2
LETC(CG iter10)	4.62/7.39	369.2
LETC-nCG	4.62/7.41	4976.7
LETC-nRSVD	4.65/7.45	194.5
LETC-circulant	4.77/7.54	146.9
LETC-symmetric	4.82/7.51	148.0
LETC-FFT	4.71/7.50	133.8
LETC-GFT	4.77/7.55	641.0
LETC-ROM	4.69/7.42	146.3
LETC-SVD	4.60/7.38	176.5
LETC-SNN	4.72/7.50	345.7

We test the above model variations on Portland data and report the resulting performances and running time in Tab. 5. Among these models, LETC with CG iter3 can be viewed as the benchmark. First, by observing the results of LETC-nRSVD and LETC-nCG that are versions without numeric approximation algorithms, we can find that the numeric accelerating methods in this work, e.g., rSVD and CG, have no negative impact on kriging precision, while reducing the computational burden at some degree. Especially, the running time of LETC-nCG is prohibitive, which means that CG plays a key role in kriging scalability. By comparing the results of LETC(CG iter3) with LETC(CG iter10), an interesting observation is that the increase of iteration times of CG would not benefit the kriging accuracy in this condition. The underlying reason for this results is that Eq. (38) is highly structure so that CG could convergence with only a few iterations.

Second, model becomes much less effective when replacing the proposed spatial and temporal regularization. Model with symmetric graph Laplacian shows the worst precision. Such results indicates the necessity of taking the moving direction of traffic flow and causality of time series into consideration.

Third, by comparing different unitary transform horizontally, it is observed that the proposed TGFT is a good balance of accuracy and efficiency. FFT features fast computation by utilizing the conjugate symmetry property, but has worse completion accuracy. GFT shows inferior performances on both precision and time cost. Since the GFT is conducted on the 'location' mode, the tensor SVT needs to be computed a large number of times, which is not cost-effective for network-wide applications. It is noteworthy that SVD based unitary transform also gives competitive results. This method obtains the transform operator by a data-driven and

iterative way, which requires more data and time cost to update the transform matrix. In addition, as SVD needs to be performed on each unfolding matrix, SNN requires more computation resources to converge and shows inferior accuracy than TNN. This observation is consistent with the findings in (Lu et al., 2019b). Overall, TGFT offers an explainable tool to perform TNN minimization, while at the same time keeps high accuracy and efficiency. Ones can incorporate prior knowledge (e.g., periodicity property) about spatiotemporal traffic data into tensor completion through TGFT.

5.3.2. Influence of graph partitioning

One significant superiority of LETC is that it can achieve efficient kriging at network-wide and one may wonder why the scalability of kriging model is important from the perspective of algorithmic performance. To demonstrate the necessity and significance of kriging on large-scale data, in this section we conduct experiments on different data size using both of the two datasets. Specifically, we adopt the same graph partitioning method as in (Chen et al., 2021a) to divide the adjacent matrices in $\{1, 2, 4, 8, 16, 32, 64\}$ parts for PeMS data and $\{1, 2, 4, 8, 16, 32\}$ parts for Portland data. The more partitions, the less data scale of each group. In each division case, we conduct kriging on all partitions and record the accuracy and running time of the whole data.

Figs. 11 and 12 show the changes of kriging performances of our LETC and another baseline method TGMF with the increase of graph partitions (decrease of data scales). As can be seen, for both of the two data, the kriging accuracy of LETC and TGMF decrease remarkably and the best performances are achieved when there is no partitioning. The reasons to explain this phenomenon could be twofold: 1) Previous study (Chen et al., 2021a) has demonstrated that low-rank tensor completion model could achieve better performances on randomly missing data imputation tasks when the data size is large. And in this work, we aim at kriging with incomplete observations and the t-TNN minimization part of our model could benefit from large data scale and learn a better low-rank pattern from a wider range. 2) The spatial graph Laplacian is at the core of kriging model, and it is directly obtained from the network topology structure. When the network is larger, more complicated and comprehensive spatial relations are incorporated in adjacent matrix and the influence of local anomaly can be weakened. Therefore, for unobserved locations there are more informative neighborhoods to provide referable observations when the network is larger.

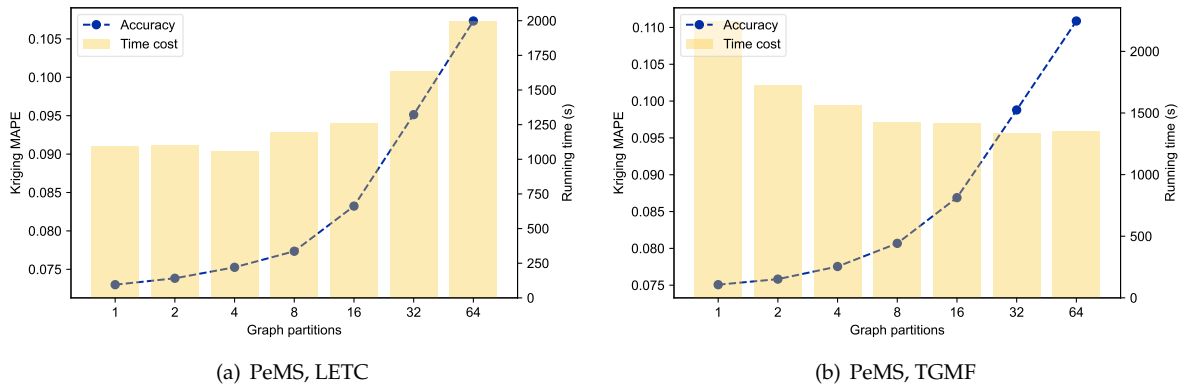


Figure 11: Model performances under different graph partitions on PeMS-4W data. (a) The proposed LETC. (b) TGMF model. The kriging accuracy and running time are both shown in this figure.

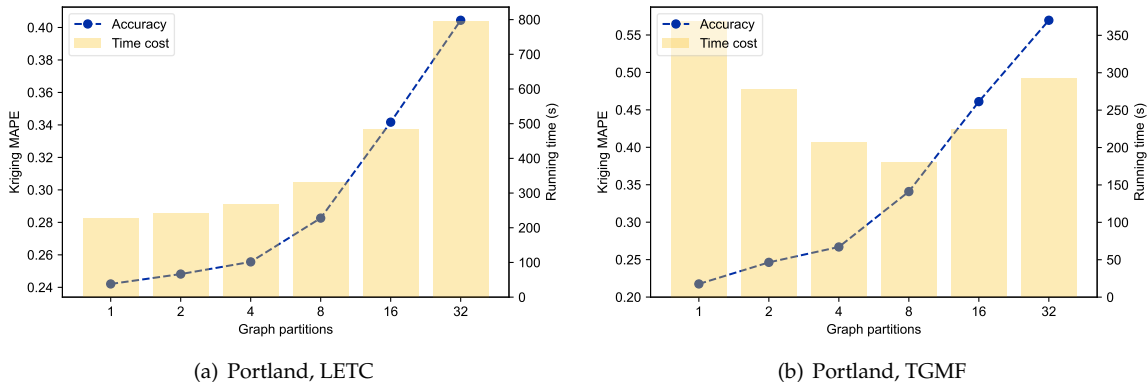


Figure 12: Model performances under different graph partitions on Portland data. (a) The proposed LETC. (b) TGMF model. The kriging accuracy and running time are both shown in this figure.

Another important observation is that the running time of LETC also gradually increases with more partitions, while the results of TGMF is quite different. Generally speaking, LETC entails the least computation cost when there exists no partitioning while it becomes the largest for TGMF in this situation. This may stem from the reason that LETC can reduce the rank of any arbitrary tensor size in the objective function, but TGMF with a fixed rank settings can not adapt to varying input data size.

Therefore, above results reveal that the proposed LETC that has better kriging scalability than other baseline models is very suitable for large-scale kriging and the motivations behind kriging at network-wide are consideration of both efficiency and precision.

5.3.3. Sensitivity analysis of hyper-parameter

It is generally acknowledged that the hyper-parameter tuning is a long-standing topic in machine learning communities. Most recently, some newly emerged Bayesian hyper-parameter optimization framework has been successfully applied to tensor/matrix factorization models to alleviate this problem (Lei et al., 2022; Chen et al., 2022b). However, learning the model hyper-parameters on network-wide data set may be quite difficult. In this work, two main hyper-parameters of LETC that have obvious impact on kriging precision are the regularization factors λ_1 and λ_2 . To discuss about the influence of λ_1 and λ_2 , we examine the model performances under different parameter settings. Moreover, another potential factor that may affect the sensitivity is the size of input data, we also take it into consideration.

In LETC, the relative magnitudes of λ_1 and λ_2 can make a difference. So we fix $\lambda_1 = 0.1$ and then set $\rho = \lambda_2/\lambda_1$ as $\{0.01, 0.05, 0.1, 0.5, 1, 5\}$. We expect to show that the influence of data scale on hyper-parameter sensitivity, so we adopt the same graph partitions on Portland data as in section 5.3.2 and for each partition group we conduct kriging using all six settings of ρ . Note that only the impact of λ_2 is discussed here as λ_2 controls the spatial regularization degree, but similar results can be observed by simply fixing λ_2 and varying λ_1 .

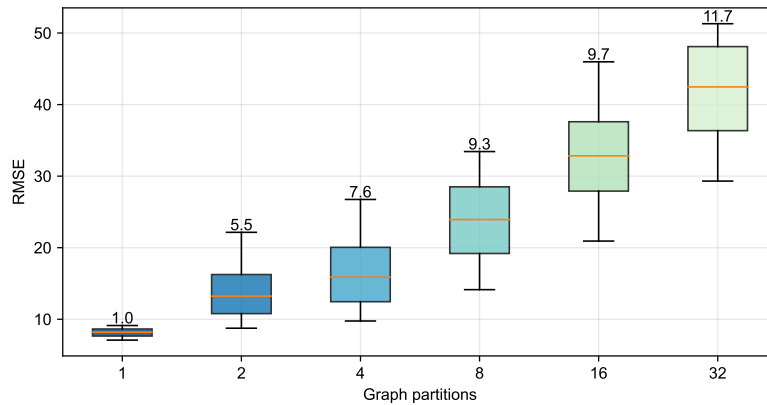


Figure 13: Sensitivity of hyper-parameters under different settings and data scales. The number on the top of each box denotes the IQR.

Fig. 13 gives the box plot for the LETC performances of all ρ setting groups under 6 data scales. Of this figure, each box represents a series of kriging results using different ρ settings on this number of graph partition. We also report the interquartile range (IQR) as a quantitative description, which is defined by the difference between the third and first quartile of each group.

There are two observations from Fig. 13: (1) The RMSE mean value (orange line in this figure) of each group monotonously increases as the partitions increase, and this result is the same as in Section 5.3.2; (2) If we define the IQR as the parameter sensitivity, it is noteworthy that the sensitivity reduces dramatically as the data scale becomes larger and the distance between the upper bound and lower bound of the box also reflects this trend. As a consequence, although we need to specify the model hyper-parameters for LETC without a hyper-parameter learning procedure, we could avoid laborious parameter tuning process on network-wide kriging task because the influence of λ_1 and λ_2 is marginal when kriging on the whole network. In practice, one can obtain the best parameter settings on a small subset of target dataset using cross-validation or grid search techniques and transfer them to the whole data directly, to seek for better model performances.

More results about model parameter sensitivity are discussed in Appendix C.

6. Conclusion and future directions

Sparse sensor coverage and data corruption inhibit availability of fine-grained and network-wide traffic speed data for transportation managements. To cope with this issue, we propose a Laplacian enhanced low-rank tensor completion (LETC) based kriging model which features both low-rankness and multi-dimensional correlations for network-wide traffic speed kriging under limited observations. Three types of speed correlation: temporal

continuity, temporal periodicity, and spatial proximity are carefully chosen and modeled by three forms of graph Laplacian. Specifically, the temporal periodicity is encoded by a new temporal graph Fourier transform (TGFT) and thus the tensor nuclear norm minimization problem can be solved in parallel by an array of daily subproblem. Considering the directional nature of traffic flow and traffic network, a novel diffusion graph regularization (DGR) is developed to model spatial proximity. To encourage time series continuity, we introduce a generalized temporal consistency regularization (GTCR). To further adapt for large-scale data, two efficient numeric techniques including conjugate gradient (CG) and randomized tensor singular value thresholding (r-tSVD) algorithm are applied to reduce the computational complexity. By performing experiments on two public million-level traffic speed datasets, we can draw the following conclusion:

1. Our proposed LETC model reconstructs more realistic temporal and spatial patterns of traffic speed than competing models, thereby achieving state-of-the-art kriging performances even with low observation rates, while at the same time saving more than half computing time compared with baseline methods;
2. Model ablation studies demonstrate the effectiveness of each model component as well as the accelerating techniques. Especially, the use of DGR and GTCR benefits the kriging precision significantly, and TNN minimization induced by TGFT maintains high accuracy, efficiency and better interpretability;
3. The sensitivity of LETC hyper-parameters is marginal on large-scale data and can be tuned in an easy routine. Moreover, this work also provides new insights into spatiotemporal traffic data kriging at network level: making fewer efforts to divide dataset could benefit both efficiency and accuracy.

There are some directions worth an extension. First, the model performance is dependent on the calculation of adjacent matrix, where a Gaussian kernel is directly used in this work. It is promising to learn an adaptive adjacent matrix from the raw location information to improve the performance. Second, we only conduct kriging for traffic speed, as the distance based adjacent relationships are practicable for loop speed. However, for trajectory based speed or traffic volume, this assumption may not work. How to achieve accurate kriging for traffic volume is a open question.

Appendix A.

Main hyper-parameter settings for LETC and other baseline models are given as follows: the convergence threshold ϵ for all above models is set to 10^{-3} . For LETC, we set the regularization parameter μ initializing with 10^{-3} and updating in each iteration with $\mu = \min\{1.5 \times \mu, 10^4\}$. The regularization parameters λ_1, λ_2 are selected from cross-validations with $\lambda_1 = 0.01$ and $\lambda_2 = 0.1$. For both PeMS and Portland data, we set $\tau = 1, 2, 3$ and report corresponding results. For LSTM-GRMF, TGMF and KPMF, a pre-specified rank is necessary, we set it as 60 for Portland data and 200 for PeMS data. For FMDT-Tucker, we set the delay parameter $\tau = [128, 256, 1]$ for Portland and $[64, 32, 1]$ for PeMS. The initial rank parameter is set to 10. As for GLTL, the orthogonal projection strategy is adopted in these experiments. For both of the two data, we compute the spatial adjacent matrix by Eq. (18), and prepare the symmetric one for baseline models by selecting the maximum values of its transpose and itself. For PeMS data, the distance matrix is based on travel distance, while coordinate position distance is adopted for Portland data. For GLOSS, we consider graph Laplacian on mode 1 and mode 2 unfoldings. And we set the Lagrange penalty parameter $\beta_1 = \beta_2 = \beta_3 = \beta = 10^{-3}, \psi_1 = \psi_2 = \psi_3 = \frac{1}{3}$. As for WDG-CP, the rank is set to 20 for Portland data and 60 for PeMS data. The graph regularization parameter is selected the same as TGMF, and the sparsity parameter is chosen as 1000 according to their work.

Appendix B.

Supplementary figures of kriging results on PeMS networks, different time slots from Fig. 9 are given as follows.

Appendix C.

We also conduct sensitivity studies on another two hyper-parameters, i.e., the Gaussian kernel parameter σ in Eq. (18), and the rank parameter k for rSVD in Algorithm 2.

In general, the Gaussian distance function is given as:

$$a_{ij}^s = \exp\left(-\left(\frac{\text{dist}(v_i, v_j)}{\delta\sigma}\right)^2\right),$$

where δ is a scale parameter needs to be tuned. Similar to the practice in section 5.3.3, we set δ as $\{0.5, 0.75, 1.0, 1.5, 2.0, 2.5\}$ and test LETC performances under different graph partitions. Each box in Fig. 15 reports the results of all parameter settings under certain graph partition.

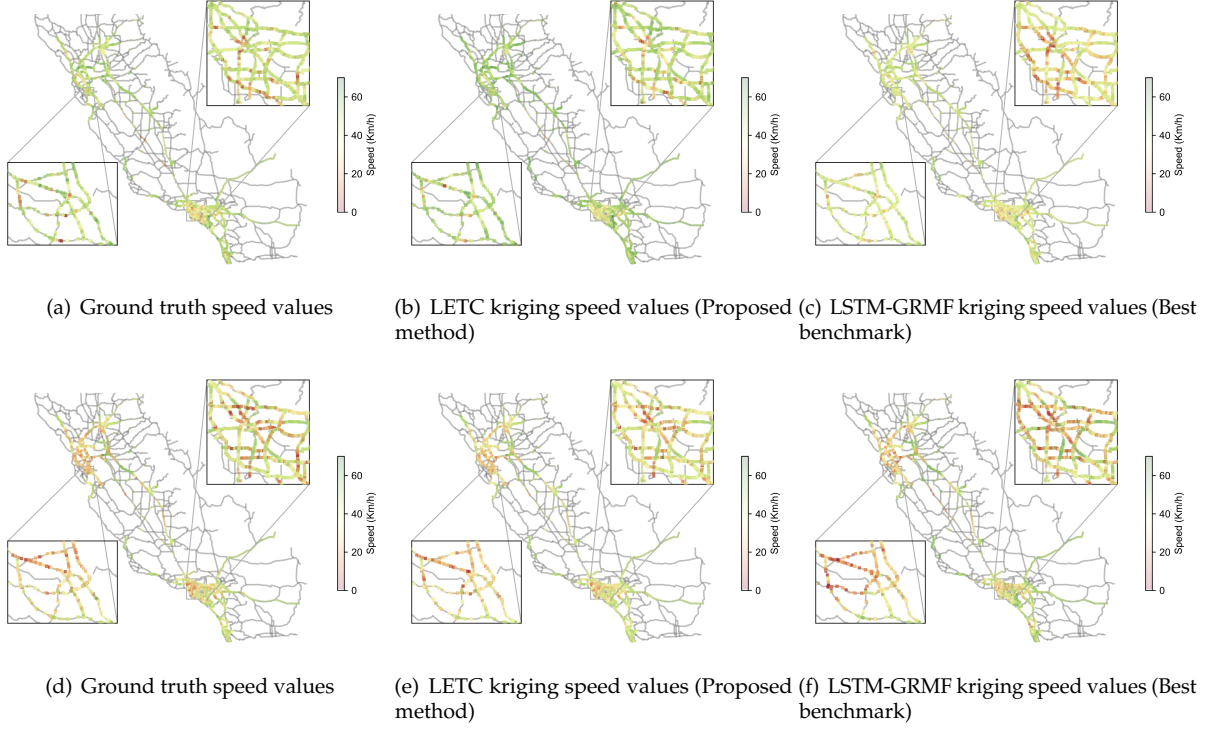


Figure 14: Supplementary figures of kriging results on PeMS networks. Results on two different time slots are plotted. (a)-(c): 14:30 P.M., (d)-(f): 17:30 P.M.

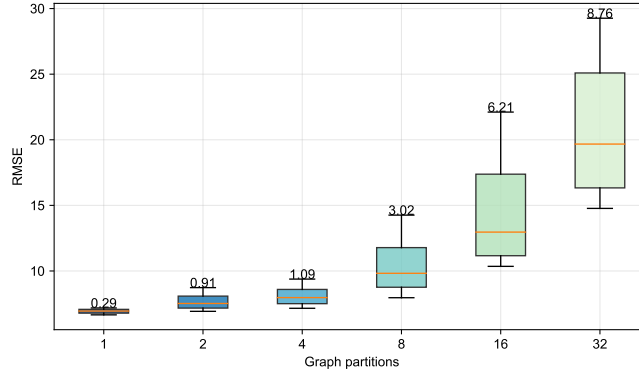


Figure 15: Sensitivity of kernel function under different settings and data scales. The number on the top of each box denotes the IQR.

As we can see, model shows varying performances with different δ values, which is consistent with the findings in the literature (Lei et al., 2022; Chen et al., 2022b). Nevertheless, by reducing the number of graph partition, the range of fluctuation denoted by IQR decreases drastically, showing similar trends to λ in section 5.3.3. As a consequence, it is not necessary to conduct hyper-parameter learning on such large-scale dataset, as the benefits could be less significant.

Rank value k in rSVD is supposed to control the convergence speed. In our implementation, we set a small initial value at first, then increase it per iteration. When the whole LETC algorithm converges, k is usually convergent. Therefore, this value mainly affects the convergence speed, has minor impacts on solving accuracy. Fig. 16 shows LETC performances with different rank initial and increment values. From these results, it is preferable to set a small value initially, and then increase it with large step.

Appendix D.

In this section we give detailed derivation of closed-form solution to problem (25). To ease the presentation, we consider the fully-observed case and assume the graph to be symmetric (similar conclusions can be draw for other settings), and the objective can be rearranged as follows:

$$\bar{\mathbf{X}} = \arg \min_{\bar{\mathbf{X}}} \|\bar{\mathbf{X}} - \mathbf{X}\|_{\mathbf{D}}^2 + \text{Tr}(\bar{\mathbf{X}}^{\top} \mathbf{L} \bar{\mathbf{X}}).$$

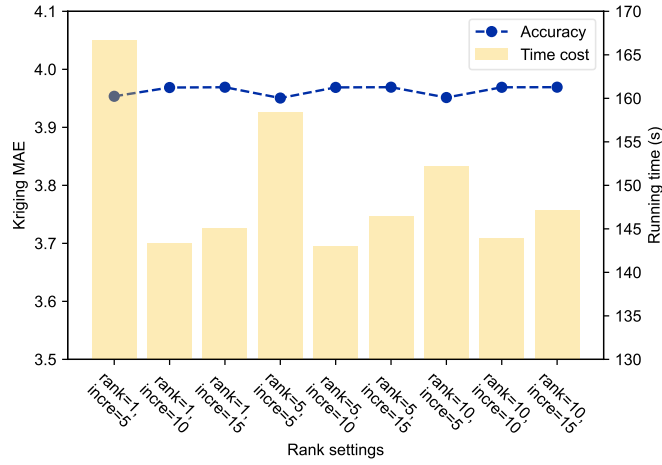


Figure 16: Model performances under different rSVD rank settings.

By setting the gradient of $\bar{\mathbf{X}}$ to zero, we have:

$$\begin{aligned}
& (\mathbf{D} + \mathbf{D}^T)(\bar{\mathbf{X}} - \mathbf{X}) + (\mathbf{L} + \mathbf{L}^T)\bar{\mathbf{X}} = 0, \\
& \Rightarrow (\mathbf{I} + \mathbf{D}^{-1}\mathbf{L})\bar{\mathbf{X}} = \mathbf{X}, \\
& \Rightarrow \bar{\mathbf{X}} = (\mathbf{I} + \tilde{\mathbf{L}})^{-1}\mathbf{X}.
\end{aligned}$$

Acknowledgement

This research was sponsored by the National Natural Science Foundation of China (52125208), and the Science and Technology Commission of Shanghai Municipality (No. 22dz1203200).

References

- Appleby, G., Liu, L., Liu, L.-P., 2020. Kriging convolutional networks. In: Proceedings of the AAAI Conference on Artificial Intelligence. Vol. 34. pp. 3187–3194.
- Asif, M. T., Mitrovic, N., Dauwels, J., Jaillet, P., 2016. Matrix and tensor based methods for missing data estimation in large traffic networks. *IEEE Transactions on intelligent transportation systems* 17 (7), 1816–1825.
- Bahadori, M. T., Yu, Q. R., Liu, Y., 2014. Fast multivariate spatio-temporal analysis via low rank tensor learning. In: *Advances in Neural Information Processing Systems*. pp. 3491–3499.
- Belkin, M., Niyogi, P., 2004. Semi-supervised learning on riemannian manifolds. *Machine learning* 56, 209–239.
- Boriboonsomsin, K., Barth, M. J., Zhu, W., Vu, A., 2012. Eco-routing navigation system based on multisource historical and real-time traffic information. *IEEE Transactions on Intelligent Transportation Systems* 13 (4), 1694–1704.
- Chamberlain, B., Rowbottom, J., Gorinova, M. I., Bronstein, M., Webb, S., Rossi, E., 2021. Grand: Graph neural diffusion. In: *International Conference on Machine Learning*. PMLR, pp. 1407–1418.
- Chen, X., Chen, Y., Saunier, N., Sun, L., 2021a. Scalable low-rank tensor learning for spatiotemporal traffic data imputation. *Transportation Research Part C: Emerging Technologies* 129, 103226.
- Chen, X., Cheng, Z., Saunier, N., Sun, L., 2022a. Laplacian convolutional representation for traffic time series imputation. *arXiv preprint arXiv:2212.01529*.
- Chen, X., Lei, M., Saunier, N., Sun, L., 2021b. Low-rank autoregressive tensor completion for spatiotemporal traffic data imputation. *IEEE Transactions on Intelligent Transportation Systems*, 1–10.
- Chen, Y., Cheng, L., Wu, Y.-C., 2022b. Bayesian low-rank matrix completion with dual-graph embedding: Prior analysis and tuning-free inference. *arXiv preprint arXiv:2203.10044*.
- Chung, F., 2005. Laplacians and the cheeger inequality for directed graphs. *Annals of Combinatorics* 9, 1–19.
- Deng, L., Liu, X.-Y., Zheng, H., Feng, X., Chen, Y., 2021. Graph spectral regularized tensor completion for traffic data imputation. *IEEE Transactions on Intelligent Transportation Systems*, 1–15.
- Golub, G. H., Van Loan, C. F., 2013. *Matrix computations*. JHU press.
- Halko, N., Martinsson, P.-G., Tropp, J. A., 2011. Finding structure with randomness: Probabilistic algorithms for constructing approximate matrix decompositions. *SIAM review* 53 (2), 217–288.

- Han, X., Shen, G., Yang, X., Kong, X., 2020. Congestion recognition for hybrid urban road systems via digraph convolutional network. *Transportation Research Part C: Emerging Technologies* 121, 102877.
- Kalofolias, V., Bresson, X., Bronstein, M., Vandergheynst, P., 2014. Matrix completion on graphs. *arXiv preprint arXiv:1408.1717*.
- Kipf, T. N., Welling, M., 2016. Semi-supervised classification with graph convolutional networks. *arXiv preprint arXiv:1609.02907*.
- Kolda, T. G., Bader, B. W., 2009. Tensor decompositions and applications. *SIAM review* 51 (3), 455–500.
- Kondor, R. I., Lafferty, J., 2002. Diffusion kernels on graphs and other discrete structures. In: *Proceedings of the 19th international conference on machine learning*. Vol. 2002. pp. 315–322.
- Lei, M., Labbe, A., Wu, Y., Sun, L., 2022. Bayesian kernelized matrix factorization for spatiotemporal traffic data imputation and kriging. *IEEE Transactions on Intelligent Transportation Systems*, 1–13.
- Li, Y., Yu, R., Shahabi, C., Liu, Y., 2017. Diffusion convolutional recurrent neural network: Data-driven traffic forecasting. *arXiv preprint arXiv:1707.01926*.
- Li, Z., Sergin, N. D., Yan, H., Zhang, C., Tsung, F., 2020. Tensor completion for weakly-dependent data on graph for metro passenger flow prediction. In: *proceedings of the AAAI conference on artificial intelligence*. Vol. 34. pp. 4804–4810.
- Liang, W., Li, Y., Xie, K., Zhang, D., Li, K.-C., Souri, A., Li, K., 2022. Spatial-temporal aware inductive graph neural network for c-its data recovery. *IEEE Transactions on Intelligent Transportation Systems*.
- Liebig, T., Piatkowski, N., Bockermann, C., Morik, K., 2017. Dynamic route planning with real-time traffic predictions. *Information Systems* 64, 258–265.
- Liu, G., Zhang, W., 2022. Recovery of future data via convolution nuclear norm minimization. *IEEE Transactions on Information Theory* 69 (1), 650–665.
- Liu, J., Han, K., Chen, X. M., Ong, G. P., 2019. Spatial-temporal inference of urban traffic emissions based on taxi trajectories and multi-source urban data. *Transportation Research Part C: Emerging Technologies* 106, 145–165.
- Liu, J., Musialski, P., Wonka, P., Ye, J., 2013. Tensor completion for estimating missing values in visual data. *IEEE Transactions on Pattern Analysis and Machine Intelligence* 35 (1), 208–220.
- Lu, C., Feng, J., Chen, Y., Liu, W., Lin, Z., Yan, S., 2016. Tensor robust principal component analysis: Exact recovery of corrupted low-rank tensors via convex optimization. In: *Proceedings of the IEEE conference on computer vision and pattern recognition*. pp. 5249–5257.
- Lu, C., Feng, J., Chen, Y., Liu, W., Lin, Z., Yan, S., 2019a. Tensor robust principal component analysis with a new tensor nuclear norm. *IEEE transactions on pattern analysis and machine intelligence* 42 (4), 925–938.
- Lu, C., Peng, X., Wei, Y., 2019b. Low-rank tensor completion with a new tensor nuclear norm induced by invertible linear transforms. In: *Proceedings of the IEEE/CVF Conference on Computer Vision and Pattern Recognition*. pp. 5996–6004.
- Luttinen, J., Ilin, A., 2009. Variational gaussian-process factor analysis for modeling spatio-temporal data. *Advances in neural information processing systems* 22.
- Meng, C., Yi, X., Su, L., Gao, J., Zheng, Y., 2017. City-wide traffic volume inference with loop detector data and taxi trajectories. In: *Proceedings of the 25th ACM SIGSPATIAL International Conference on Advances in Geographic Information Systems*. pp. 1–10.
- Nie, T., Qin, G., Sun, J., 2022. Truncated tensor Schatten p-norm based approach for spatiotemporal traffic data imputation with complicated missing patterns. *Transportation Research Part C: Emerging Technologies* 141, 103737.
- Nt, H., Maehara, T., 2019. Revisiting graph neural networks: All we have is low-pass filters. *arXiv preprint arXiv:1905.09550*.
- Page, L., Brin, S., Motwani, R., Winograd, T., 1998. The pagerank citation ranking: Bring order to the web. *Tech. rep., technical report, Stanford University*.
- Rao, N., Yu, H.-F., Ravikumar, P. K., Dhillon, I. S., 2015. Collaborative filtering with graph information: Consistency and scalable methods. *Advances in neural information processing systems* 28.
- Sandryhaila, A., Moura, J. M., 2013. Discrete signal processing on graphs: Graph fourier transform. In: *2013 IEEE International Conference on Acoustics, Speech and Signal Processing*. IEEE, pp. 6167–6170.
- Shi, Q., Yin, J., Cai, J., Cichocki, A., Yokota, T., Chen, L., Yuan, M., Zeng, J., 2020. Block hankel tensor arima for multiple short time series forecasting. In: *Proceedings of the AAAI Conference on Artificial Intelligence*. Vol. 34. pp. 5758–5766.
- Shuman, D. I., Narang, S. K., Frossard, P., Ortega, A., Vandergheynst, P., 2013. The emerging field of signal processing on graphs: Extending high-dimensional data analysis to networks and other irregular domains. *IEEE signal processing magazine* 30 (3), 83–98.
- Singh, R., Chakraborty, A., Manoj, B., 2016. Graph fourier transform based on directed laplacian. In: *2016 International Conference on Signal Processing and Communications (SPCOM)*. IEEE, pp. 1–5.
- Sofuoglu, S. E., Aviyente, S., 2022. Gloss: Tensor-based anomaly detection in spatiotemporal urban traffic data. *Signal Processing* 192, 108370.
- Song, G., Ng, M. K., Zhang, X., 2020. Robust tensor completion using transformed tensor singular value decomposition. *Numerical Linear Algebra with Applications* 27 (3), e2299.
- Strahl, J., Peltonen, J., Mamitsuka, H., Kaski, S., 2020. Scalable probabilistic matrix factorization with graph-based priors. In: *Proceedings of the AAAI Conference on Artificial Intelligence*. Vol. 34. pp. 5851–5858.

- Tan, H., Feng, G., Feng, J., Wang, W., Zhang, Y.-J., Li, F., 2013. A tensor-based method for missing traffic data completion. *Transportation Research Part C: Emerging Technologies* 28, 15–27.
- Wang, X., Miranda-Moreno, L., Sun, L., 2021a. Hankel-structured tensor robust pca for multivariate traffic time series anomaly detection. *arXiv preprint arXiv:2110.04352*.
- Wang, X., Wu, Y., Zhuang, D., Sun, L., 2021b. Low-rank hankel tensor completion for traffic speed estimation. *arXiv preprint arXiv:2105.11335*.
- Wang, Y., Zhang, Y., Piao, X., Liu, H., Zhang, K., 2018. Traffic data reconstruction via adaptive spatial-temporal correlations. *IEEE Transactions on Intelligent Transportation Systems* 20 (4), 1531–1543.
- Wu, Y., Zhuang, D., Labbe, A., Sun, L., 2021a. Inductive graph neural networks for spatiotemporal kriging. In: *Proceedings of the AAAI Conference on Artificial Intelligence*. Vol. 35. pp. 4478–4485.
- Wu, Y., Zhuang, D., Lei, M., Labbe, A., Sun, L., 2021b. Spatial aggregation and temporal convolution networks for real-time kriging. *arXiv preprint arXiv:2109.12144*.
- Wu, Z., Pan, S., Long, G., Jiang, J., Zhang, C., 2019. Graph wavenet for deep spatial-temporal graph modeling. *arXiv preprint arXiv:1906.00121*.
- Xu, B., Shen, H., Cao, Q., Cen, K., Cheng, X., 2020. Graph convolutional networks using heat kernel for semi-supervised learning. *arXiv preprint arXiv:2007.16002*.
- Yamamoto, R., Hontani, H., Imakura, A., Yokota, T., 2022. Fast algorithm for low-rank tensor completion in delay-embedded space. In: *Proceedings of the IEEE/CVF Conference on Computer Vision and Pattern Recognition*. pp. 2058–2066.
- Yang, J.-M., Peng, Z.-R., Lin, L., 2021. Real-time spatiotemporal prediction and imputation of traffic status based on lstm and graph laplacian regularized matrix factorization. *Transportation Research Part C: Emerging Technologies* 129, 103228.
- Yang, L., Fang, J., Duan, H., Li, H., Zeng, B., 2018. Fast low-rank bayesian matrix completion with hierarchical gaussian prior models. *IEEE Transactions on Signal Processing* 66 (11), 2804–2817.
- Yokota, T., Erem, B., Guler, S., Warfield, S. K., Hontani, H., 2018. Missing slice recovery for tensors using a low-rank model in embedded space. In: *IEEE Conference on Computer Vision and Pattern Recognition*. pp. 8251–8259.
- Yu, H.-F., Rao, N., Dhillon, I. S., 2016. Temporal regularized matrix factorization for high-dimensional time series prediction. *Advances in neural information processing systems* 29.
- Zhang, J., Saibaba, A. K., Kilmer, M. E., Aeron, S., 2018. A randomized tensor singular value decomposition based on the t-product. *Numerical Linear Algebra with Applications* 25 (5), e2179.
- Zhang, Z., Li, M., Lin, X., Wang, Y., 2020. Network-wide traffic flow estimation with insufficient volume detection and crowdsourcing data. *Transportation Research Part C: Emerging Technologies* 121, 102870.
- Zhou, T., Shan, H., Banerjee, A., Sapiro, G., 2012. Kernelized probabilistic matrix factorization: Exploiting graphs and side information. In: *Proceedings of the 2012 SIAM international Conference on Data mining*. SIAM, pp. 403–414.